



SFERA II

Solar Facilities for the European Research Area

Contract n° GA 312643

SFERA II Project

Solar Facilities for the European Research Area

Document Title	D15.8 : Report on solids as sensible heat storage materials
Revision	
Diffusion date	17/01/2017
WP	15
Author(s)	A. Steinfeld, ETH Zurich T. Esence, J.F. Fourmigué CEA Liten
Verification	

Project co-funded by the European Commission within the Seventh Framework Programme (2007-2013)		
Dissemination Level		
PU	Public	x
PP	Restricted to other programme participants (including the Commission Services)	
RE	Restricted to a group specified by the consortium (including the Commission Services)	
CO	Confidential, only for members of the consortium (including the Commission Services)	

For EC Approval

Date

Name

Signature

SFERA II Project:

Start date 1 January 2014

End date 31 December 2017

WP15 Task3.4, Task leader ENEA



Summary

Part 1 : Experimental studies about solid sensible heat storage and feedback	3
Experimental applications.....	3
Heat transfer fluid	9
Solid material tank filling	9
References.....	11
Part 2 : Example of thermocline-type TES using rocks and encapsulated PCM	13
Abstract.....	13
Nomenclature	13
Introduction	15
Prototype Design	17
Modeling	23
Experimental Results and Model Validation	27
Summary and Conclusions	31
References.....	32



Part 1 : Experimental studies about solid sensible heat storage and feedback

Authors : T. Esence, J.F. Fourmigué, CEA Liten

In this part, the main experimental setups are briefly presented and feedback of the experimental studies is discussed in terms of system performances, operation and design. Finally, the main characteristics and some key aspects of filler materials and HTF are presented.

Experimental applications

Some of the most relevant packed-bed storage installations with liquid or gaseous HTF are listed in Table 1 and Table 2 respectively. It should be noticed that some characteristics of the referenced systems are not directly available in the original papers. Some of them were easily deduced and calculated from given data, while the others were estimated from partial data. The former are indicated with one asterisk (*) and the latter with two asterisks (**).

The first full-scale industrial packed bed for CSP storage was implemented in 1982 in Solar One (Faas et al., 1986; McDonnell Douglas Astronautics Company, 1986). Solar One was a 10-MW_e CSP tower plant using water as HTF and integrating a 182-MWh_{th} storage of more than 3,000 m³ composed of a mixture of rocks and sand with oil up to 290°C as HTF. It was rapidly shut down (in 1986) due to accidental admission of water in the tank which caused sudden pressure elevation and tank damage. As preparatory work on Solar One, a similar pilot-scale 5.7-MWh_{th} storage was tested (Hallet and Gervais, 1977). From these two experiments only partial data and little feedback are available in the literature.

More detailed experimental results are available from the work of Pacheco et al., 2002, who tested a 2.3-MWh_{th} storage of about 40 m³ comprised of rocks and sand with molten salt up to 390 °C as HTF. Nowadays this reference paper is used by many authors to validate numerical models (Bayón and Rojas, 2013; Flueckiger et al., 2014; Van Lew et al., 2011; Xu et al., 2012). However, exhaustive operative conditions used during tests were not published, and available temperature profiles suffer from significant and unexplained scattering.

In addition to these two well-known experimental setups, some other pilot-scale packed-bed storages have been implemented and tested.

Zanganeh et al., 2012, built a 6.5-MWh_{th} rock-bed storage running up to 500 °C with air as HTF. This truncated conical bed was buried to tackle thermomechanical stresses on the walls. The authors used the experimental results to validate a numerical model and to design the full-scale storage of the 3.9-MW_{th} parabolic trough CSP plant of Aït-Baha (Morocco) which started production in 2014 (Airlight Energy; Zanganeh et al., 2014). Since Solar One, this is probably the first commercial CSP plant with packed-bed storage. It consists of a pebble bed with air as HTF (Zanganeh et al., 2014) similar to the one presented and designed in Zanganeh et al., 2012. As far as the authors know, no operational data have been published so far.

Kuravi et al., 2013, implemented a structured packed bed of bricks of about 0.1 m³ with air up to 530 °C as HTF. They confirmed the viability of structured packed beds in terms of fluid distribution and thermal stratification and validated a numerical model with the experimental data.

The experimental studies carried out by CEA (Bruch et al., 2014a; Bruch et al., 2014b; Bruch et al., 2017; Rodat et al., 2015) investigated the behavior of packed beds of 2.4 and 30 m³ comprised of rocks and sand with thermal oil up to 300 °C as HTF. The experimental results show smooth temperature profiles, with low experimental scattering, and exhibit a very repeatable and robust stabilized state through various flow and temperature conditions fixed by the operator. The studies highlight in particular the influence of various cycling conditions on packed-bed performances.

This behavior through charge and discharge cycles was also observed by Cascetta et al., 2015, on a 0.5-m³ packed bed of alumina beads with air up to 240 °C. The authors investigated the influences of aspect ratio (i.e. height-to-diameter ratio of the bed), air flow rate, temperature level and inertia of the walls (highlighted by radial temperature profiles) on the storage performances.



Except the above mentioned installations, most of the experimental data available in the literature come from laboratory-scale setups. These experiments enable to investigate some phenomena but are often non-representative of the overall behavior of large size installations (Fig. 1).

For example, heat losses are proportionally higher in small tanks due to higher surface-to-volume ratio. Despite thermal insulation, several small size installations showed significant thermal losses which affected experimental results (Hoffmann et al., 2016; Klein et al., 2013; Kuravi et al., 2013; Okello et al., 2014; Shewen et al., 1978). As an example, the experimental system studied by Okello et al., 2014 (about 0.05 m³), lost about 25 % of its energy content during a 18-h standby period, while the Solar One's TES (more than 3,000 m³) lost only 2.5 % of its energy content in 20 h (Faas et al., 1986) with similar average temperature.

Besides, absolute and relative dimensions of the tank and the solid particles of the bed influence flow distribution and velocity profiles, thereby affecting heat exchange and thermal stratification in the storage. In small tanks, the relative influence of the walls over velocity profiles is higher than in large tanks due to edge effects. Flow channeling near the walls is also influenced by the tank-to-particle diameter ratio.

Proportion effects may also affect laboratory-scale experiments. While the height occupied by the thermocline, which affects storage behavior and efficiency, is relatively thin in industrial-scale or pilot-scale systems, many laboratory-scale results show thermocline which occupies the whole height of the storage during charge or discharge (Anderson et al., 2014; Bhavsar and Balakrishnan, 1990; Mawire and Taole, 2011; Meier et al., 1991; Shitzer and Levy, 1983; Yang et al., 2014).

In these conditions, experimental results from laboratory-scale systems should be considered with precaution because their behavior and their performances may significantly differ from industrial-scale.

The following picture summarize the different packed-bed heat storage systems showing that if a lot of lab-scale examples exists only a few ones have near commercial scales dimensions.

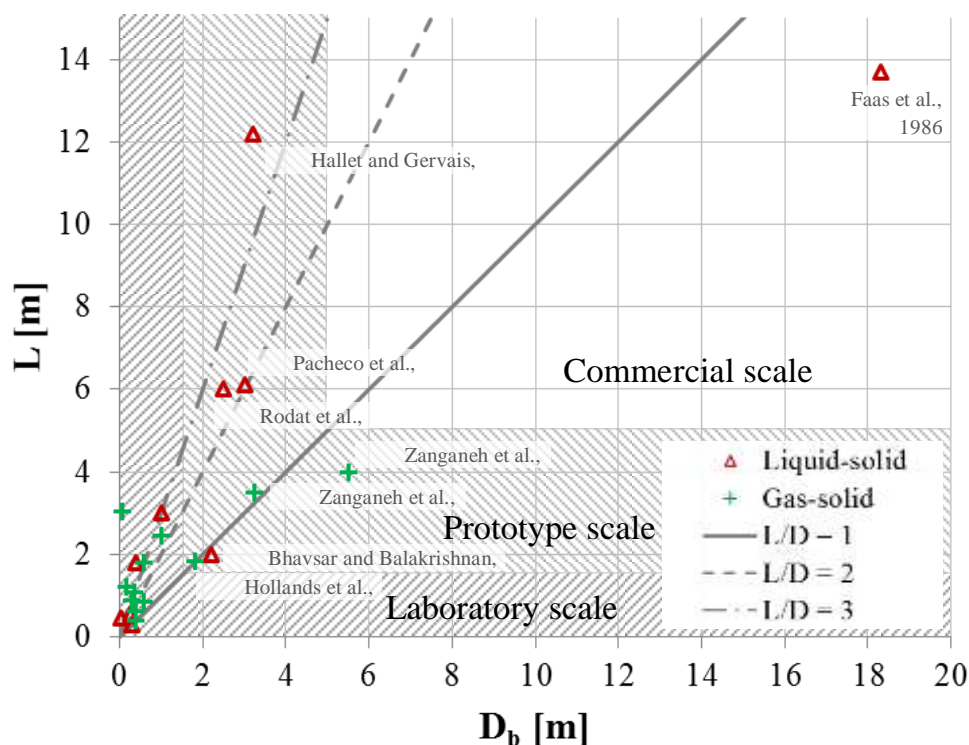


Fig. 1. Dimensions of referenced packed-bed storage systems.



SFERA II - PROJECT

Solar Facilities for the European Research Area

Publications	Solid	Fluid	D_b (m)	L (m)	D_s (mm)	ϵ	D_b/D_s	T (°C)	u	Packed-bed temperature measurements
Hallet and Gervais, 1977	River gravels (granite) and silica sand	Caloria HT 43 (oil)	3.2	12.2	25 / 1.5	0.25	128	218 - 302	0.3 – 3.3 mm/s *	Fluid Axial / Radial
Faas et al., 1986; McDonnell Douglas Astronautics Company, 1986	Rocks and sand	Caloria HT 43 (oil)	18.3	13.7	25 / -	0.22	732	200 - 290	-	Fluid Axial
Bhavsar and Balakrishnan, 1990	Rocks	HP Hytherm 500 (oil)	2.2	2.0	50	0.30	44	230 - 247	0.4 mm/s *	Fluid / Solid Axial / Radial
Pacheco et al., 2002	Quartzite rocks and silica sand	Hitec XL [®] (Ca(NO ₃) ₂ -NaNO ₃ - KNO ₃ , 42-15-43 wt %)	3.0	6.1	19 / -	0.22	158	290 - 390	2.6 mm/s **	Fluid Axial / Radial
Mawire et al., 2009; Mawire and McPherson, 2009; Mawire and Taole, 2011	Sandy stones	CALFLO [™] LT (oil)	0.29	0.3	5	0.42	58	20 - 240	0.04 – 0.12 mm/s *	Fluid Axial
Mawire et al., 2010	Silica glass pebbles	Shell Therma Oil B (oil)	0.035	0.45	3	0.42	12	30 - 160	10 – 19 mm/s *	Fluid Axial
Yang et al., 2014	Ceramic spheres	Hitec [®] (KNO ₃ -NaNO ₂ -NaNO ₃ , 53-40-7 wt %)	0.263	0.55	30	-	8.8	280 - 355	3 mm/s **	Fluid Axial
Bruch et al., 2014a; Bruch et al., 2017	Silica gravels and silica sand	Therminol [®] 66 (oil)	1.0	3.0	30 / 3	0.27	33	50 - 250	0.7 – 2.8 mm/s ***	Fluid / Solid Axial / Radial
Rodat et al., 2015	Silica gravels and silica sand	Therminol [®] 66 (oil)	2.5	6.0	30 / 3	0.27	83	100 - 250	0.5 – 1.7 mm/s	Fluid / Solid Axial / Radial
Hoffmann et al., 2016	Quartzite rocks	Rapeseed oil	0.4	1.8	40	0.41	4.5	160 - 210	0.5 mm/s *	Fluid Axial / Radial

Table 1. Main characteristics of some liquid/solid packed-bed storage applications from the literature.



SFERA II - PROJECT

Solar Facilities for the European Research Area

Publications	Solid	Fluid	D_b (m)	L (m)	D_s (mm)	ϵ	D_p/D_s	T (°C)	u	Packed-bed temperature measurements
Hollands et al., 1984; Shewen et al., 1978	River gravels	Air	1.8×1.8	0.38 – 1.82	18.1	0.42	99	20 - 67	15 – 30 cm/s **	Fluid / Solid Axial / Radial
Coutier and Farber, 1982	Rocks	Air	0.57	0.84	18 – 28	-	20 – 32	-	-	Fluid / Solid Axial / Radial
Shitzer and Levy, 1983	Crushed quarry rocks	Air	1.0	2.45	18 – 45	0.34	22.2 – 55.6	30 - 75	20 – 46 cm/s **	Fluid / Solid Axial
Beasley and Clark, 1984	Soda lime glass spheres	Air	0.375	0.62	12.6	0.364	30	25 - 70	40 – 300 cm/s **	Fluid / Solid Axial / Radial
Meier et al., 1991	Porcelain spheres	Air	0.15	1.20	20	0.40	7.5	25 - 550	90 cm/s	Fluid Axial
Zanganeh et al., 2012	Sedimentary rocks	Air	2.5 – 4	2.9	20 - 30	0.342	83 - 200	20 - 500	3.0 cm/s **	Fluid Axial
Klein et al., 2013	Ceramic balls	Flue gas / air	0.40	0.62	19	0.39	21	25 - 900	90 – 140 cm/s **	Fluid / Solid Axial / Radial
Kuravi et al., 2013	Bricks	Air	0.508×0.203	1.07	$50.8 \times 203 \times 178$	0.20	-	20 - 530	510 – 590 cm/s **	Fluid / Solid Axial / Radial
Okello et al., 2014	Crushed rocks	Air	0.40 0.40	0.40 0.90	14.6	0.38	27	20 - 350	12 cm/s ** 22 cm/s **	Fluid Axial
Anderson et al., 2014	Alumina spheres	Air	0.572	3.05	6	0.40	20	25 - 120	485 – 975 cm/s *	Fluid Axial
Zanganeh et al., 2014	Rocks	Air	5 – 6	4.0	-	-	-	250 - 550	-	Fluid Axial / Radial
Cascetta et al., 2015	Sintered alumina beads	Air	0.58	1.80	7 - 9	0.39	64.5 – 83.0	38 - 239	90 – 225 cm/s **	Fluid Axial / Radial

Table 2. Main characteristics of some gas/solid packed-bed storage applications from the literature.

* recalculated value

** estimated value from partial data

*** there is a subscript mistake in Bruch et al., 2017: the velocity values correspond to interstitial velocities (and not to superficial velocities)

The following table (table3) presents the physical properties of the solid heat storage materials used in the different setups presented in figure1.



SFERA II - PROJECT

Solar Facilities for the European Research Area

Publications	Solid filler material	Solid density ($\text{kg}\cdot\text{m}^{-3}$)	Solid specific heat capacity ($\text{J}\cdot\text{kg}^{-1}\cdot\text{K}^{-1}$)	Solid thermal conductivity ($\text{W}\cdot\text{m}^{-1}\cdot\text{K}^{-1}$)
Hallet and Gervais, 1977	Rocks and sand	2650	1035	-
Faas et al., 1986; McDonnell Douglas Astronautics Company, 1986	River gravels (granite) and silica sand	2645	1020	-
Bhavsar and Balakrishnan, 1990	Rocks	-	-	-
Pacheco et al., 2002	Quartzite rocks and silica sand	2500 **	850 **	-
Mawire et al., 2009; Mawire and McPherson, 2009; Mawire and Taole, 2011	Sandy stones	2800	745	2
Mawire et al., 2010	Silica glass pebbles	2465	790	-
Yang et al., 2014	Ceramic spheres	2100	-	-
Bruch et al., 2014a; Bruch et al., 2017	Silica gravels and silica sand	2500	900	-
Rodat et al., 2015	Silica gravels and silica sand	2500	900	-
Hoffmann et al., 2016	Quartzite rocks	2500	830	5.7
Hollands et al., 1984; Shewen et al., 1978	River gravels	2690	920	-
Coutier and Farber, 1982	Rocks	-	-	-
Shitzer and Levy, 1983	Crushed quarry rocks	-	-	-
Beasley and Clark, 1984	Soda lime glass spheres	2485	775	-
Meier et al., 1991	Porcelain spheres	-	-	-
Zanganeh et al., 2012	Sedimentary rocks	2735	655	2.6
Klein et al., 2013	Ceramic balls	2200	1115	1.3



SFERA II - PROJECT

Solar Facilities for the European Research Area

Kuravi et al., 2013	Bricks	3200	800	1.6
Okello et al., 2014	Crushed rocks	-	880	-
Anderson et al., 2014	Alumina spheres	3685	840	28.5
Zanganeh et al., 2014	Rocks	-	-	-
Cascetta et al., 2015	Sintered alumina beads	3550	902	-

Table 3. Main characteristics materials used in experimental setups.

** estimated value from partial data



Heat transfer fluid

In most cases, liquid HTF consists either of thermal oil or molten nitrate salts, while gaseous HTF consists of air (sometimes of flue gas for high temperature tests). Physical properties at average operating temperature of some typical HTF are presented in Table 4. In particular, the volumetric heat capacity ($\rho \cdot c_p$) enables to assess the heat storage density of materials, while the thermal effusivity E enables to assess their ability to exchange heat.

Liquid HTF have good heat capacity and thermal conductivity compared to gasses. This enables liquid/solid systems to operate at low HTF velocity while keeping a good heat transfer coefficient (HTC), which improves thermal stratification. Moreover, liquids have a high viscosity compared to gasses, which leads to low Reynolds number. As flow dispersion is low at small Reynolds numbers (Yang and Garimella, 2010), stratification is generally better in liquid/solid systems, thereby improving efficiency of the storage. Besides, due to poor thermal properties of gasses, gas/solid systems require to operate at high flow rate, otherwise charging and discharging would be unacceptably long. However, this may lead to non-negligible pressure losses and hence energy consumption due to high pumping costs of compressible fluids (Kuravi et al., 2013).

On the other hand, air is free, non-toxic and non-flammable, which may significantly reduce installation costs and safety concerns. Moreover, air is chemically stable and can operate at very high temperature, thus increasing energy density of the storage and efficiency of the electric conversion. The chemical compatibility between the fluid and the solids is usually less problematic with air than with oils or molten salts.

Fluid	T_{\min}/T_{\max} (°C)	ρ (kg·m ⁻³)	c_p (J·kg ⁻¹ ·K ⁻¹)	λ (W·m ⁻¹ ·K ⁻¹)	μ (Pa·s)	$\rho \cdot c_p$ (kWh·m ⁻³ ·K ⁻¹)	E (J·K ⁻¹ ·m ⁻² ·s ^{-1/2})
Caloria HT 43	0 / 315	695	2700	0.16	$6.8 \cdot 10^{-4}$	0.52	547
Therminol 66	0 / 345	845	2380	0.10	$5.7 \cdot 10^{-4}$	0.56	451
Jarytherm DBT	0 / 350	870	2350	0.11	$4.7 \cdot 10^{-4}$	0.57	469
Solar salt	220 / 600	1835	1510	0.52	$1.8 \cdot 10^{-3}$	0.77	1200
Hitec	142 / 535	1790	1560	0.33	$1.8 \cdot 10^{-3}$	0.78	960
Hitec XL	120 / 500	1990	1445	0.52	$6.3 \cdot 10^{-3}$	0.80	1224
Water	0 / 100	990	4180	0.64	$5.8 \cdot 10^{-4}$	1.15	1627
Air	- / -	0.5	1075	0.05	$3.4 \cdot 10^{-5}$	$1.5 \cdot 10^{-4}$	5.3

Table 4. Physical properties of some usual HTF at average operating temperature.

Solid material tank filling

Coming from different authors, physical properties of some representative sensible heat storage solids, from natural to recycled ones, are presented in Table 5. These values are estimated since they depend on the quality and the origin of materials. This table shows the large range of heat storage density but this aspect have to be considered in regard of cost an availability.



Solid	ρ (kg·m ⁻³)	c_p (J·kg ⁻¹ ·K ⁻¹)	λ (W·m ⁻¹ ·K ⁻¹)	$\rho \cdot c_p$ (kWh·m ⁻³ ·K ⁻¹)	E (J·K ⁻¹ ·m ⁻² ·s ^{-1/2})
Quartzite	2600	850	5.5	0.61	3486
Basalt	2900	900	2.0	0.73	2285
Concrete	2200	850	1.5	0.52	1675
Bricks	3200	800	1.6	0.71	2024
Ceramic	3550	900	1.3	0.89	2038
Alumina	4000	900	11	1.0	6293
Cofalit (asbestos waste)	3120	982	1.5	0.85	2144
blast furnace slag	2980	996	3	0.82	2984

Table 5. Order of magnitude of physical properties of some sensible heat storage solids.

Packed bed can be made of either structured or non-structured solid filler. Non-structured filler enables to use low cost solids like pebbles. If a single size of spheroidal solids is used, void fraction of the bed is typically around 0.3-0.4 (Nellis and Klein, 2009). A void fraction around 0.25 can be achieved by using two sizes of particle, e.g. by mixing rocks and sand (Bruch et al., 2014a; Faas et al., 1986; Hallet and Gervais, 1977; Pacheco et al., 2002). The decrease in void fraction enables to decrease the cost of liquid/solid systems since liquid HTF are often more expensive than the solids chosen for thermal storage applications. In gas/solid systems, reducing the void fraction enables to improve the storage density of the system since the volumetric heat capacity of solids is much higher than the one of gases. However this method increases interstitial velocity of the fluid and pressure loss which may be restrictive when using gaseous HTF. Manufactured materials like ceramic, glass or alumina, usually of spherical shape, may be used in order to run at very high temperature or to prevent fluid/solid chemical interactions. Small solid size is preferable to improve stratification since it increases the total fluid/solid heat exchange area and reduces the Biot number of solids (Van Lew et al., 2011; Yang and Garimella, 2010). For stratification purpose, Biot number of the particles has to be as low as possible so that heat transfer is only governed by convection (Adeyanju and Manohar, 2009), resulting in a sharper thermal front and better stratification. This influence was illustrated by both numerical models (Durisch et al., 1986; Mertens et al., 2014; Yang and Garimella, 2010) and experimental studies (Anderson et al., 2014). As long as fluidization is avoided, reducing particle size also improves flow uniformity by increasing pressure loss (Hollands et al., 1984) and by preventing flow channeling near the walls. In cylindrical beds, this latter phenomenon can be avoided by respecting a minimum tank-to-particle diameter ratio of 30-40 (Meier et al., 1991; Rose and Rizk, 1949). In the case of rectangular cross section, the ratio between the smaller side of the tank and the solid diameter has to be greater than 50 to avoid wall channeling (Hollands et al., 1984).

Structured filler material, like bricks or plates, may be used to shape the bed. Although this is more expensive, this enables to optimize the geometry of the bed in terms of heat exchange, conduction resistance of the solid and pressure losses. Low void fraction can be reached (e.g. 0.2 for Kuravi et al., 2013) while keeping acceptable pressure loss. Furthermore, structured filler material enables to tackle with the near-wall channeling issue and to prevent reorganization of solids over thermal cycles, which is very likely to solve the great mechanical concern of thermal ratcheting. For all these reasons, structured filler is particularly suitable with gaseous HTF operated at high temperature.



References

- Adeyanju, A.A., Manohar, K., 2009. Theoretical and experimental investigation of heat transfer in packed beds, *Res.J.Appl.Sci.*, vol. 4, 166 - 177.
- Allen K.G., T.W.vonBackström, D.G.Kröger, A.F.M.Kisters, 2014. Rock bed storage for solar thermal power plants: Rock characteristics, suitability, and availability, *Solar Energy Materials & Solar Cells* 126, 170–183
- Airlight Energy. Ait-Baha CSP pilot plant. <http://www.airlightenergy.com/ait-baha-csp-pilot-plant/>, Apr. 2016.
- Anderson, R., Shiri, S., Bindra, H., Morris, J.F., 2014. Experimental results and modeling of energy storage and recovery in a packed bed of alumina particles, *Appl.Energy*, vol. 119, 521 - 529.
- Bayón, R., Rojas, E., 2013. Simulation of thermocline storage for solar thermal power plants: From dimensionless results to prototypes and real-size tanks, *Int.J.Heat Mass Transf.*, vol. 60, 713 - 721.
- Beasley, D.E., Clark, J.A., 1984. Transient response of a packed bed for thermal energy storage, *Int.J.Heat Mass Transf.*, vol. 27, 1659 - 1669.
- Bhavsar, V.C., Balakrishnan, A.R., 1990. Pebble bed-oil thermal energy storage for solar thermo-electric power systems, *Int J Energy Res*, vol. 14, 233 - 240.
- Bruch, A., Fourmigué, J.F., Couturier, R., 2014a. Experimental and numerical investigation of a pilot-scale thermal oil packed bed thermal storage system for CSP power plant, *Sol.Energy*, vol. 105, 116 - 125.
- Bruch, A., Fourmigué, J. F., Couturier, R., Molina, S., 2014b. Experimental and numerical investigation of stability of packed bed thermal energy storage for CSP power plant, *SolarPACES 2013, Energy Procedia*, vol. 49, 743 - 751.
- Bruch, A., Molina, S., Esence, T., Fourmigué, J.F., Couturier, R., 2017. Experimental investigation of cycling behaviour of pilot-scale thermal oil packed-bed thermal storage system, *Renewable Energy*, vol. 103, 277 - 285.
- Cascetta, M., Cau, G., Puddu, P., Serra, F., 2015. Experimental investigation of a packed bed thermal energy storage system, *J.Phys.Conf.Ser.*, vol. 655.
- Coutier, J.P., Farber, E.A., 1982. Two applications of a numerical approach of heat transfer process within rock beds, *Sol.Energy*, vol. 29, 451 - 462.
- Durisch, W., Frick, E., Kesselring, P., 1986. Heat Storage in solar power plants using solid beds, *High temperature technology and its applications, Solar thermal central receiver systems : proceedings of the third international workshop*, vol. 2, 879 - 896.
- Faas, S.E., Thorne, L.R., Fuchs, E.A., Gilbertsen, N.D., 1986. 10 Mwe Solar Thermal Central Receiver Pilot Plant - Thermal storage subsystem evaluation - Final report, SAND86-8212.
- Flueckiger, S.M., Iverson, B.D., Garimella, S.V., Pacheco, J.E., 2014. System-level simulation of a solar power tower plant with thermocline thermal energy storage, *Appl.Energy*, vol. 113, 86 - 96.
- Grirate H, H. Agalit, N. Zari, A. Elmchaouri, S. Molina, R. Couturier 2016. Experimental and numerical investigation of potential filler Solar Energy 131 260–274
- materials for thermal oil thermocline storage
- Hallet, R.W.Jr., Gervais, R.L., 1977. Central receiver solar thermal power system - Phase 1 - CDRL ITEM 2 - Pilot Plant Preliminary Design Report - Vol V - Thermal Storage Subsystem, SAN/1108-8/5.
- Hoffmann, J.F., Fasquelle, T., Goetz, V., Py, X., 2016. A thermocline thermal energy storage system with filler materials for concentrated solar power plants: Experimental data and numerical model sensitivity to different experimental tank scales, *Appl Therm Eng*, vol. 100, 753 - 761.
- Hollands, K.G.T., Sullivan, H.F., Shewen, E.C., 1984. Flow uniformity in rock beds, *Sol.Energy*, vol. 32, 343 - 348.
- Klein, P., Roos, T. H., Sheer, T. J., 2013. Experimental investigation into a packed bed thermal storage solution for solar gas turbine systems, *SolarPACES 2013, Energy Procedia*, vol. 49, 840 - 849.
- Kuravi, S., Trahan, J., Goswami, Y., Jotshi, C., Stefanakos, E., Goel, N., 2013. Investigation of a high-temperature packed-bed sensible heat thermal energy storage system with large-sized elements, *J Sol Energy Eng Trans ASME*, vol. 135.
- Mawire, A., McPherson, M., 2009. Experimental and simulated temperature distribution of an oil-pebble bed thermal energy storage system with a variable heat source, *Appl Therm Eng*, vol. 29, 1086 - 1095.
- Mawire, A., McPherson, M., van den Heetkamp, R.R.J., Mlatho, S.J.P., 2009. Simulated performance of storage materials for pebble bed thermal energy storage (TES) systems, *Appl.Energy*, vol. 86, 1246 - 1252.
- Mawire, A., McPherson, M., van den Heetkamp, R.R.J., Taole, S.H., 2010. Experimental volumetric heat transfer characteristics between oil and glass pebbles in a small glass tube, *Energy*, vol. 35, 1256 - 1263.

SFERA II - PROJECT



Solar Facilities for the European Research Area

-
- Mawire, A., Taole, S.H., 2011. A comparison of experimental thermal stratification parameters for an oil/pebble-bed thermal energy storage (TES) system during charging, *Appl.Energy*, vol. 88, 4766 - 4778.
- McDonnell Douglas Astronautics Company, 1986. 10 MWe Solar Thermal Central Receiver Pilot Plant Mode 5 (Test 1150) and Mode 6 (Test 1160) Test report, Sandia National Laboratories, SAND86-8175.
- Meier, A., Winkler, C., Wuillemin, D., 1991. Experiment for modelling high temperature rock bed storage, *Solar Energy Materials*, vol. 24, 255 - 264.
- Mertens, N., Alobaid, F., Frigge, L., Epple, B., 2014. Dynamic simulation of integrated rock-bed thermocline storage for concentrated solar power, *Sol.Energy*, vol. 110, 830 - 842.
- Nellis, G., Klein, S., 2009. *Heat Transfer*. Cambridge, 1107 p.
- Okello, D., Nydal, O.J., Banda, E.J.K., 2014. Experimental investigation of thermal de-stratification in rock bed TES systems for high temperature applications, *Energy Convers.Manage.*, vol. 86, 125 - 131.
- Pacheco, J.E., Showalter, S.K., Kolb, W.J., 2002. Development of a molten-salt thermocline thermal storage system for parabolic trough plants, *J Sol Energy Eng Trans ASME*, vol. 124, 153 - 159.
- Rodat, S., Bruch, A., Dupassieux, N., Mourchid, N. E., 2015. Unique Fresnel Demonstrator Including ORC and Thermocline Direct Thermal Storage: Operating Experience, *Energy Procedia*, vol. 69, 1667 - 1675.
- Rose, H.E., Rizk, A.M.A., 1949. Further Researches in Fluid Flow through Beds of Granular Material, *Proc.Inst.Mech.Eng.*, vol. 160, 493 - 503.
- Shewen, E.C., Sullivan, H.F., Hollands, K.G.T., Balakrishnan, A.R., 1978. A heat storage subsystem for solar energy - Final report - Phase 2, STOR - 6.
- Shitzer, A., Levy, M., 1983. Transient Behavior of a Rock-Bed Thermal Storage System Subjected to Variable Inlet Air Temperatures - Analysis and Experimentation, *J Sol Energy Eng Trans ASME*, vol. 105, 200 - 206.
- Van Lew, J.T., Li, P., Chan, C.L., Karaki, W., Stephens, J., 2011. Analysis of heat storage and delivery of a thermocline tank having solid filler material, *J Sol Energy Eng Trans ASME*, vol. 133, 021003-1 - 021003-10.
- Xu, C., Wang, Z., He, Y., Li, X., Bai, F., 2012. Sensitivity analysis of the numerical study on the thermal performance of a packed-bed molten salt thermocline thermal storage system, *Appl.Energy*, vol. 92, 65 - 75.
- Yang, X., Qin, F.G.F., Jiang, R., 2014. Experimental investigation of a molten salt thermocline storage tank, *Int.J.Sustainable Energy*.
- Yang, Z., Garimella, S.V., 2010. Thermal analysis of solar thermal energy storage in a molten-salt thermocline, *Sol.Energy*, vol. 84, 974 - 985.
- Zanganeh, G., Ambrosetti, G., Pedretti, A., Zavattoni, S., Barbato, M., Good, P., Haselbacher, A., Steinfeld, A., 2014. A 3 MWth parabolic trough CSP plant operating with air at up to 650 °C, *Proc.Int.Renew.Sustain.Energy Conf.*, 108 - 113.
- Zanganeh, G., Pedretti, A., Zavattoni, S., Barbato, M., Steinfeld, A., 2012. Packed-bed thermal storage for concentrated solar power - Pilot-scale demonstration and industrial-scale design, *Sol.Energy*, vol. 86, 3084 - 3098.



Part 2 : Example of thermocline-type TES using rocks and encapsulated PCM

Author: A. Steinfeld, ETH Zurich

The following report is based on 3 refereed journal papers:

1. Zanganeh G., Khanna R., Walser C., Pedretti A., Haselbacher A., Steinfeld A., “Experimental and Numerical Investigation of Combined Sensible-Latent Heat for Thermal Energy Storage at 575 °C and above”, *Solar Energy*, Vol. 114, pp. 77-90, 2015.
2. Geissbühler L., Zavattoni S., Barbato M., Zanganeh G., Haselbacher A., Steinfeld A., “Experimental and Numerical Investigation of Combined Sensible/Latent Thermal Energy Storage for High-Temperature Applications”, *Chimia*, Vol. 69, pp. 799–803, 2015.
3. Geissbühler L., Kolman M., Zanganeh G., Haselbacher A., Steinfeld A., “Analysis of industrial-scale high-temperature combined sensible/latent thermal energy storage”, *Applied Thermal Engineering*, Vol. 101, pp. 657–668, 2016.
- 4.

Abstract

The design, testing, and modelling of a high-temperature thermocline-type thermal energy storage (TES) are presented. The TES concept uses air as the heat-transfer fluid and combines sensible and latent heat for stabilizing the discharging outflow air temperature. A 42 kWh_{th} lab-scale prototype was fabricated, cylindrical in shape with 40 cm diameter, and containing 9 cm-height of encapsulated phase change material (AlSi₁₂) on top of 127 cm-height packed bed of approximately 3 cm diameter sedimentary rocks. A two-phase transient heat transfer model of the thermal storage cycle was numerically formulated and experimentally validated with measured thermoclines during charging and discharging obtained with the lab-scale prototype. Thermal inertia of the experimental setup and radial variation of void fraction due to the small tank-to-particle diameter ratio affected the validation process. The outflow air temperature during discharging was stabilized around the melting temperature of AlSi₁₂ of 575 °C. The thermal losses stayed below 3.5% of the input energy for all the experimental runs.

Nomenclature

Latin characters

A	Surface area	[m ²]
a	Surface area per unit volume	[m ² /m ³]
C	Heat capacity	[J/kgK]
d	Diameter	[m]
E	Thermal capacity, Thermal energy	[kWh]
e	Internal energy	[J/kg]
f	Fraction	[-]
G	Mass flow rate per unit cross section	[kg/m ² s]
H	Height	[m]
h	Specific enthalpy of fluid	[J/kg]

SFERA II - PROJECT



Solar Facilities for the European Research Area

	Heat transfer coefficient	[W/m ² K]
h_{fus}	Heat of fusion	[J/kg]
h_p	Particle convective heat transfer coefficient	[W/m ² K]
h_v	Volumetric convective heat transfer coefficient	[W/ m ³ K]
k	Thermal conductivity	[W/mK]
m	Mass	[kg]
\dot{m}	Mass flow rate	[kg/s]
Q	Heat flux	[W]
r	Radius	[m]
S_D	Longitudinal pitch	[m]
S_T	Transverse pitch	[m]
T	Temperature	[K] or [°C]
t	Time	[s]
	Thickness	[m]
u	Interstitial velocity	[m/s]
u_0	Superficial velocity	[m/s]
V	Volume	[m ³]
x	Axial coordinate	[m]

Greek characters

ε	Void fraction	[-]
ϵ	Emissivity	[-]
μ	Dynamic viscosity	[kg/ms]
ρ	Density	[kg/m ³]
σ	Stefan-Boltzmann constant, $5.6704 \cdot 10^{-8}$	[W/m ² K ⁴]

Dimensionless groups

Bi	Biot number, $h_p r/ k_s$	[-]
Nu	Nusselt Number, $h_p d/ k_f$	[-]
Pe	Peclet number, $\rho C_p u d/ k_f$	[-]
Pr	Prandtl number, $C_p \mu/ k$	[-]
Re	Reynolds number for PCM tubes, $\rho u_{max} d/ \mu$	[-]
Re ₀	Superficial Reynolds number for packed bed of rocks, $\rho u_0 d/ \mu$ or Gd/ μ	[-]

Subscripts

0	Conditions of the free flow
∞	Surrounding
c	Circumferential
ch	Charging



<i>cond</i>	Conduction
<i>cont</i>	Contact
<i>dis</i>	Discharging
<i>eff</i>	Effective
<i>enc</i>	Encapsulation
<i>f</i>	Fluid
<i>fus</i>	Fusion
<i>melt</i>	Melting
<i>PCM</i>	Phase change material
<i>R</i>	Rocks
<i>rad</i>	Radiation
<i>ref</i>	Reference
<i>i</i>	Spatial increment or row number
<i>in</i>	Inside or in
<i>out</i>	Outside or out
<i>s</i>	Solid
<i>th</i>	Thermal
<i>v</i>	Volumetric

Abbreviations

CFL	Courant-Friedrichs-Lewy number
CSP	Concentrated solar power
DSC	Differential scanning calorimeter
HTF	Heat-transfer fluid
PCM	Phase change material
r.h.s.	Right hand side
TES	Thermal energy storage

Introduction

Due to the temporal shift between peak insolation and the peak electricity demand, thermal-energy storage (TES) systems are an integral part of CSP plants (Pitz-Paal et al., 2012). Reviews of TES concepts for CSP plants have been given by Herrmann and Kearney (Herrmann and Kearney, 2002), Gil et al. (Gil et al., 2010), Medrano et al. (Medrano et al., 2010), and Kuravi et al. (Kuravi et al., 2013). Current commercial CSP plants commonly employ oil, molten salt, or steam as the heat-transfer fluid (HTF) and incorporate two-tank molten salt (Reilly and Kolb, 2001), two-tank oil (Herrmann et al., 2003), one-tank steam (SOLUCAR, 2006), or oil with and without filler material (Geyer et al., 1987; Kolb et al., 1991) as TES systems. At present, air is not extensively applied as HTF in CSP plants due to its comparatively low volumetric heat capacity and thermal conductivity, which require larger heat transfer areas and volumetric flow rates. Nevertheless, air has several advantages: it is free, has no upper-temperature limitation, suffers no degradation, and is not toxic. Examples of CSP designs that use air as HTF include pressurized receivers for solar tower systems (Buck et al., 1999; Kribus et al., 2001; Heller et al., 2006; Hischer et al., 2012) and non-pressurized receivers for solar trough systems (Boyd et al., 1976; Bader et al., 2010; Good et al., 2013). Various TES concepts have been experimentally investigated for use with high-temperature air, including a packed beds of rocks (Meier et al.,



1991; Hänchen et al., 2011; Zanganeh et al., 2012), alumina porcelain ceramics (Zunft et al., 2011), or ZrO_2 pellets (Jalalzadeh-Azar et al., 1996; Nsofor and Adebisi, 2001), and a sand-based heat exchanger (Warekar et al., 2011). Particularly, rocks are cheap and usually locally available. Most of the experimental work on packed beds of rocks has been conducted for small scales and low temperatures ($T < 200$ °C) (Coutier and Farber, 1982; Shitzer and Levy, 1983; Beasley and Clark, 1984; Sorour, 1988; Jones and Golshekan, 1989). An exception is a 6.5 MWh_{th} pilot-scale demonstration unit, operated at charging temperatures up to 600 °C (Zanganeh et al., 2012) designed an air-based tubular receiver for a CSP trough system that can deliver air at 600°C and above (Good et al., 2013) Recently, rocks have been suggested as filler material for oil and molten salt tanks in order to increase the energy density and help create and maintain temperature stratification (Van Lew et al., 2011; Flueckiger et al., 2012; Valmiki et al., 2012).

Packed beds of rocks using air as HTF finds application not only in CSP plants (Bader et al., 2011), but also in adiabatic compression-expansion cycles for electricity storage (Jakiel et al., 2007). An inherent disadvantage of thermocline-type sensible-heat storage is the drop of the outflow air temperature toward the end of discharge period. This drop can be disadvantageous when integrating such storage units with downstream applications that require or benefit from steady-state conditions, e.g., Rankine and Brayton heat engines or thermochemical processes. Another disadvantage is associated with the low capacity ratio, defined as the ratio of the actually used thermal capacity of the storage stored to the maximum possible thermal capacity, but this drawback can be tolerated for low-cost storage materials such as rocks.

Latent heat storage using phase change materials (PCM), on the other hand, has somewhat higher energy density and can store and release heat at constant temperature. The use of PCM for TES has been reviewed by Zalba et al. (Zalba et al., 2003), Farid et al. (Farid et al., 2004), Kenisarin and Mahkamov (Kenisarin and Mahkamov, 2007), Agyenim et al. (Agyenim et al., 2010), Kenisarin et al. (Kenisarin, 2010), Dutil et al. (Dutil et al., 2011), Fernandes et al. (Fernandes et al., 2012), Cárdenas and León (Cárdenas and León, 2013), and Nkwetta and Haghightat (Nkwetta and Haghightat, 2014). The majority of the experimental works in the literature appear to focus on PCMs for low-temperature TES such as paraffin wax (Beasley et al., 1989; Fukai et al., 2003; Ettouney et al., 2005; Nallusamy et al., 2007; Antony Aroul Raj and Velraj, 2011). Experimental studies at high temperatures ($T > 500$ °C) include inorganic salts and metallic alloys (Yagi and Akiyama, 1995), salt/ceramic composites (Na_2SO_4/SiO_2) (Jalalzadeh-Azar et al., 1997), and Al-Si metallic alloys (He and Zhang, 2001; Wang et al., 2006; Kotzé et al., 2013a). A disadvantage of latent heat storage is its inadequacy for heat storage within a large temperature range. In fact, some studies comparing sensible and latent heat storage concluded that there is no significant improvement of the storage performance when sensible heat storage material is replaced by latent heat storage material (Jalalzadeh-Azar et al., 1997; Flueckiger and Garimella, 2014; Nkwetta and Haghightat, 2014). This might be solved by using a cascaded configuration with PCMs of different melting temperatures (Watanabe et al., 1993; Michels and Pitz-Paal, 2007; Yang and Zhang, 2012; Flueckiger and Garimella, 2014), but at the expense of complicated designs and higher costs.

A suitable PCM should exhibit the following properties (Kenisarin, 2010): 1) adequate melting temperature for the specific application; 2) high latent heat of fusion to decrease the required amount of material; 3) high thermal conductivity for rapid heat transfer across the encapsulation and for homogeneous melting/solidification; 4) low supercooling and a small phase-transition temperature range; 5) small volume expansion to reduce the risk of damaging the encapsulation; and 6) chemical stability and non-toxicity. Most of the previous work on high-temperature latent-heat storage focused on salt compositions as PCM. Metallic PCM in the form of metal alloys are attractive for high-temperature latent heat storage due to their high thermal conductivities (up to two orders of magnitude higher than those of salts), negligible supercooling, and relatively small volume change during melting (Birchenall and Riechman, 1980). Recently, a eutectic alloy containing 88% aluminum and 12% silicon by mass, frequently denoted as AlSi₁₂, with a melting temperature of about 575 °C, has been investigated (Yagi and Akiyama, 1995; He and Zhang, 2001; Wang et al., 2006; Kotzé et al., 2013a; Kotzé et al., 2013b).

Previously, a concept was proposed that combines the advantages of the sensible and latent heat storages while alleviating the critical issues incurred when using them separately (Hahne et al., 1991; Zanganeh et al., 2014). The proposed design adds a relatively small amount of encapsulated PCM on top of the packed bed of rocks as depicted in Fig. 1. During charging, hot air enters the TES from the top, transfers heat to the PCM and rocks, and exits at the bottom. During discharging the flow is reversed: air enters from the bottom, is heated by the rocks and PCM, and exits at the top. The direction of the flow exploits buoyancy forces to create and maintain thermal stratification, with the hottest region at the top of the storage tank. The effect of different PCM materials and amounts was investigated numerically (Zanganeh et al., 2014). It was found that the outflow air temperature could be stabilized around the PCM's melting point. The purpose of this paper is to present the results of the experimental investigation of the combined storage introduced above and the validation of the numerical model.

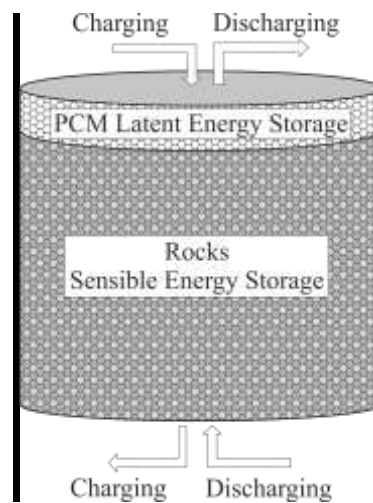


Fig. 1: Scheme of the combined sensible and latent heat concept for thermal energy storage, comprising a relatively small layer of PCM on top of a packed bed of rocks.

Prototype Design

The 42 kWh_{th} lab-scale prototype is shown in schematic form in Fig. 2.

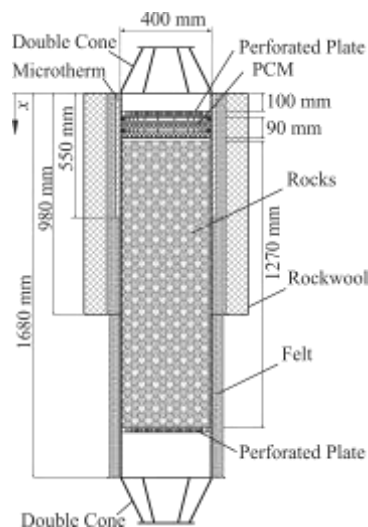


Fig. 2: Configuration of the 42 kWh_{th} lab-scale prototype used in the experimental campaign.

Configuration — Two configurations were investigated: the “rocks + PCM” setup as shown in Fig. 2, and the “rocks only” setup where the PCM is replaced by rocks, for the purpose of comparing the performance between the combined sensible/latent heat storage with the sensible heat storage only. The structure consists of a stainless steel tank (AISI 304) of 1680 mm length, 400 mm outer diameter and 3 mm thickness. 20 mm thick steel plates perforated with 221 10 mm diameter holes are welded to the tank at a distance of 200 mm from the bottom and 100 mm from the top of the tank for the purpose of creating a uniform air flow. The bottom perforated plate further supports the weight of the storage material. The rocks and encapsulated PCM are placed between the perforated plates. Steel sections with double cones are used to connect the top and bottom of the tank to the smaller delivery tubes. The storage dimensions are listed in



Table 1. The insulation materials, dimensions, and thermal conductivities are listed in Table 2, with the origin of the axial coordinate x indicated in Fig. 2. The insulation is thicker at the top than at the bottom to account for the temperature stratification.

Table 1: Dimensions and properties of the storage tank, the sensible heat and latent heat sections.

Tank Dimensions		Latent Section		Sensible Section	
		H_{PCM} [m]	0.09		
		d_{enc} [m]	0.018	H_{rocks} [m]	1.27/1.36 (“rocks only”)
		ε_{PCM} [-]	0.549	d_{rocks} [m]	0.032
r_{in} [m]	0.197	ρ_{AlSi2} [kg/m ³]	2650	ε_{rocks} [-]	0.4
r_{out} [m]	0.2	ρ_{AlSi16} [kg/m ³]	7930	k_{rocks} [W/mK]	1-5 (T -dependent)
H_{tank} [m]	1.68	h_{fus} [kJ/kg]	466	ρ_{rocks} [kg/m ³]	2635
		ΔT_{melt} [K]	4	E_{rocks} [kWh _{th}]	38.2/41 (“rocks only”)
		E_{PCM} [kWh _{th}]	3	m_{rocks} [kg]	~245/262 (“rocks only”)
		E_{enc} [kWh _{th}]	1.2		

Table 2: Insulation materials, dimensions, and thermal conductivities. Thermal conductivity values are taken from manufacturers’ data sheets.

Height [m]	Insulation Thickness [m]		Thermal Conductivity [W/mK]	
	Microtherm®/Felt/Rockwool		20°C < T < 700°C	
$x < 0.55$	0.02/0.04/0.1		$k_{microtherm}$	0.026-0.038
$0.55 < x < 0.98$	0/0.06/0.1		k_{felt}	0.046-0.078
$0.98 < x < 1.68$	0/0.05/0		$k_{rockwool}$	0.038

Sensible-heat storage section — The sensible-heat storage section consists of rocks excavated from the Rafzerfeld area near Zurich, Switzerland. The average void fraction was measured by filling the void space with water. Seven visually different rocks were chosen from the packed bed and their heat capacity was measured with differential scanning calorimetry (DSC) in the range 0 - 600 °C. The repeatability of the measurements was verified by conducting two consecutive heating and cooling cycles. The mean values for the cooling and heating runs, averaged for the seven rock types, are plotted in Fig. 3. The peak in heat capacity around 575 °C was ascribed to the α - β -inversion of quartz. The heat required to complete this inversion is 20.2 Joule per gram of quartz (Hemingway, 1987; Somerton, 1992). The heat capacity is used to calculate the internal energy of the rocks $e_s(T+\Delta T) = e_s(T) + C_s(T)\Delta T$ with a resolution of $\Delta T=5$ °C, also shown in Fig. 3. A second-order polynomial was fitted to give $e_s = aT + bT^2$, with T in °C, e_s in J/kg, $a=747.0995$, and $b=0.2838$.

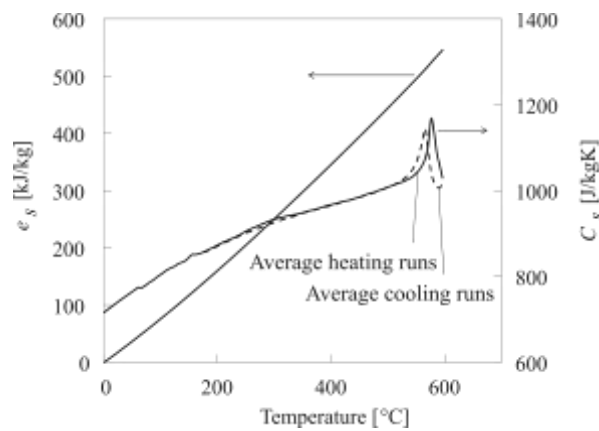


Fig. 3: Average internal energy for the heating runs ($T_{ref} = 0\text{ °C}$) and average heat capacity for the heating and cooling runs as a function of temperature, averaged for the seven rock types in the packed bed, measured using DSC.

The temperature-dependent thermal conductivity of the rocks was measured using the hot-wire method (Zanganeh et al., 2012) and is given in Table 1. The density of the rocks was measured using the Archimedes' principle (Pratten, 1981). The average density of the seven rock types is listed in

Table 1. The mean particle diameter was obtained by analyzing a photograph containing 5095 rocks (Wipware, 2013). The particle size distribution is shown in Fig. 4. The mean particle diameter was 32 mm with a standard deviation of 13.4 mm.

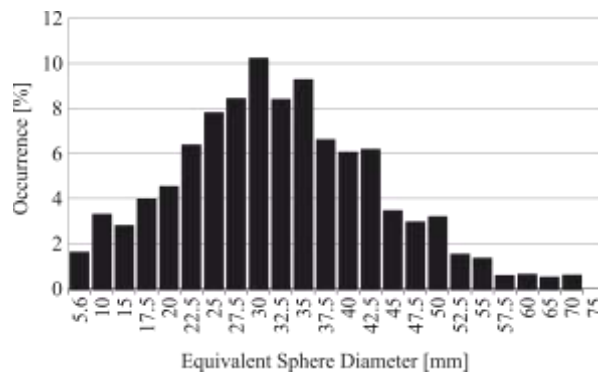


Fig. 4: Particle size distribution of the rocks used in the experimental setup.

Latent-heat storage section — The latent heat storage section is placed on top of the rocks. This section consists of the PCM AlSi_{12} encapsulated in stainless steel (AISI 316) tubes of 16 mm inner diameter and 1 mm wall thickness. The tubes were filled with molten PCM and closed by welding stainless steel caps to their ends under argon purge. They were arranged in 4 rows, each row containing 17 tubes aligned perpendicularly to the adjacent row(s), as shown in Fig. 5. This arrangement gives a total height of the latent-heat storage section of 9 cm with an average void fraction of 0.549. The masses of the PCM and the encapsulation material, as well as the total volume of the encapsulation tubes for each row are listed in Table 3.



Table 3: Mass of PCM (AlSi₁₂) and encapsulation material (AISI 316 steel), and the total volume of the encapsulation tubes in each row. Row 1 is the topmost layer and row 4 the bottom-most layer.

	Row 1	Row 2	Row 3	Row 4	Total
m_{PCM} [kg]	2.37	2.41	2.39	2.42	9.59
m_{enc} [kg]	3.29	3.29	3.29	3.30	13.17
$V_{tubes} \cdot 10^3$ [m ³]	1.237	1.238	1.237	1.241	4.953



Fig. 5: Photographs of the encapsulated PCM and the arrangement in rows.

Reported values of the heat of fusion of AlSi₁₂ varied from 460 to 560 kJ/kg (Yagi and Akiyama, 1995; He and Zhang, 2001; Wang et al., 2006; Kotzé et al., 2013a). The temperature-dependent heat capacity of the AlSi₁₂ was measured by DSC. Three consecutive heating and cooling runs at a rate of 15 K/min were carried out to ensure repeatability. Fig. 6 shows the averaged results for the solid, two-phase, and liquid states. The melting onset was observed at 571 °C and 5 °C higher than the solidifying onset at 566°C. In the solid state, the heat capacity increased from 950 J/kgK to 1190 J/kgK. In liquid state, the heat capacity was constant at around 1170 J/kgK. The heat of fusion, obtained by integration, was 466 kJ/kg. The results obtained from the DSC measurements indicate a large melting/solidification temperature range of about 50 °C, which is ascribed to the heating/cooling rates of the DSC of 15 K/min. However, congruent melting and solidification of the PCM in the range of 573-577 °C observed during the experimental campaign (see Fig. 12 c) and d)) and in preliminary tests indicates a melting/solidification range of 4 °C. Fig. 7 shows the inside wall temperature and PCM temperature at two locations inside of a tube with 2 cm diameter filled with PCM used in the preliminary tests to investigate the melting behavior in an oven. The melting temperature range is about 4 °C and the temperature differences between the tube and PCM are seen to be negligible, indicating low Biot numbers and uniform melting. Also, a study by Arkar and Medved (Arkar and Medved, 2005) on paraffin also shows that variations of the heating rate of the DSC can affect the temperature range of the phase transition. However, they do not affect the area under the curve and hence the latent heat of fusion.

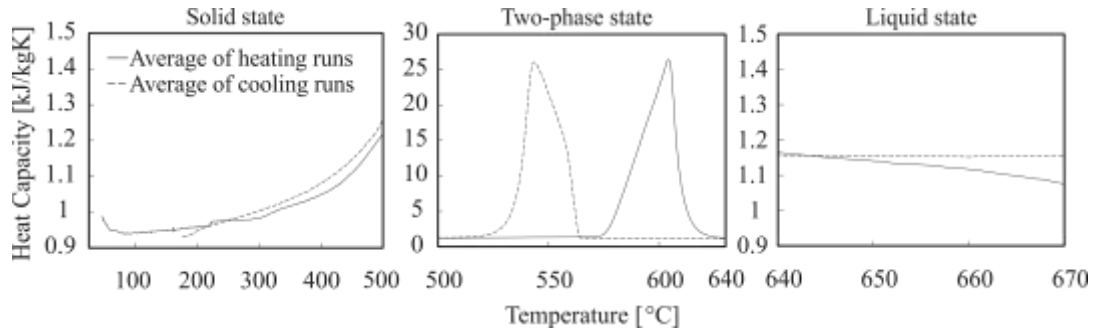


Fig. 6: Heat capacity of AlSi_{12} as a function of temperature for the solid, two-phase, and liquid states, measured using a differential scanning calorimeter, averaged for 3 heating and cooling runs.

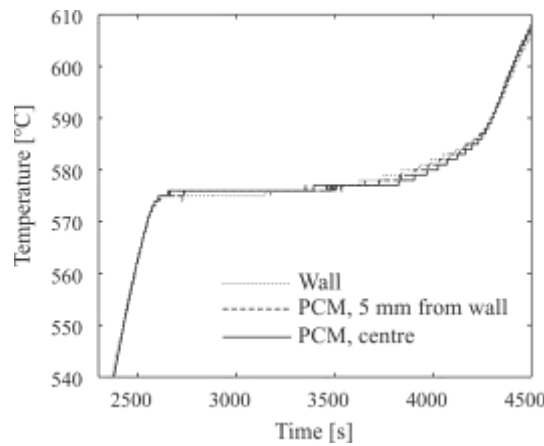


Fig. 7: Wall and PCM temperatures at two locations inside the tube used in the preliminary tests. Due to the high conductivity of the PCM, the curves mostly overlap, indicating low Biot numbers and uniform melting. The melting range is 573-577 °C.

Table 4 lists the heat capacities and thermal conductivities of the PCM and encapsulation material. Data was taken from literature (Wang et al., 2006; Incropera et al., 2007), except for the measured heat capacity of AlSi_{12} . The densities of AlSi_{12} and AISI 316 were measured and are given in Table 1.

Table 4: Heat capacity and thermal conductivity of PCM (AlSi_{12}) and encapsulation material (AISI 316 steel).

		$T < 573^\circ\text{C}$	$573^\circ\text{C} < T < 577^\circ\text{C}$	$T > 577^\circ\text{C}$	Reference
AlSi_{12}	C_{PCM} [J/kgK]*	1070	$C_{pseudo} = h_{fus} / \Delta T_{melt}$	1170	Measured by DSC (Wang et al., 2006)
	k_{PCM} [W/mK]		160		
AISI 316	C_{enc} [J/kgK]	535	581	590	(Incropera et al., 2007)
	k_{enc} [W/mK]	17.7	22	23.1	(Incropera et al., 2007)

* Experimentally measured.

The thermal capacity, defined as the total thermal energy stored when charged from ambient temperature to isothermal conditions at 650°C, was 38.2 kWh_{th} for the sensible heat storage section and 4.2 kWh_{th} for the latent heat storage section, for a total of 42.4 kWh_{th}.



Experimental setup — Fig. 8 shows a schematic of the experimental setup. During charging, ambient air circulated by the blower is first heated to 600-700 °C using a 21-kW electric heater. The hot air enters the storage at the top, transfers heat to the storage material, exits at the bottom, and finally flows through the mass flow meter before exiting the circuit. During discharging, ambient air at $T_{ambient} \approx 25$ °C flows in the opposite direction, first through the mass flow meter, then into the storage from the bottom, is heated in the storage, and exits the circuit from its top. The blower frequency and heater power are controlled and the mass flow meter and thermocouple signals are recorded.

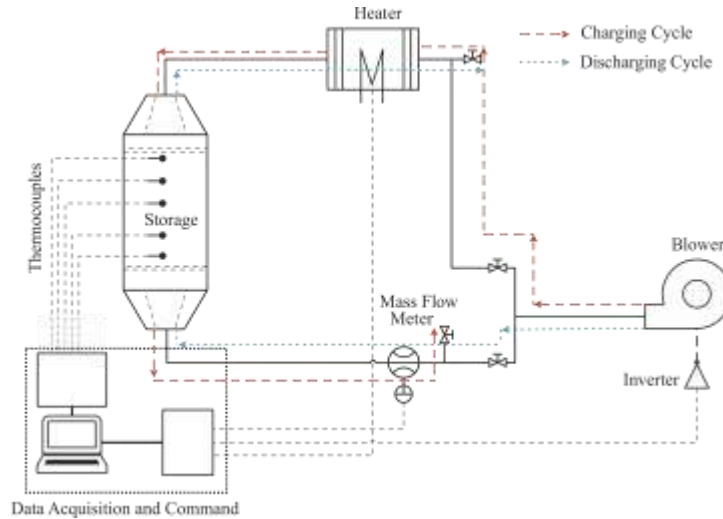


Fig. 8: Schematic of the experimental setup indicating the flow direction during charging and discharging.

In each PCM row, thermocouples are placed inside the center tube (T_{PCM}) and in the void space (T_f) to measure the PCM and air temperatures, respectively. Two thermocouples are placed on the inside of the tank wall at the height of the 2nd and 4th PCM row ($T_{wall,2}$ and $T_{wall,4}$). Further, the temperatures at the top inlet ($T_{inlet,top}$, see Fig. 9) and the bottom outlet ($T_{outlet,bottom}$, below the rocks) of the storage, as well as above the perforated plate ($T_{plate,top}$) and at the outlet of the heater (T_{Heater}) are monitored. In the sensible heat storage section, thermocouples are placed at the center of the packed bed at different heights (T_R). The position of the thermocouples for the two sets of tests is summarized in Table 5.

Table 5: Distance of the thermocouples from $T_{inlet,top}$ as shown in Fig. 9 of the storage for the two sets of tests (in mm).

Designation	rocks + PCM	rocks only
$T_{inlet,top}$	0	0
$T_{PCM,1}, T_{f,1}$	11	-
$T_{PCM,2}, T_{f,2}$	34	-
$T_{PCM,3}, T_{f,3}$	56	-
$T_{PCM,4}, T_{f,4}$	79	-
$T_{R,1}$	379	225
$T_{R,2}$	720	574
$T_{R,3}$	1045	865
$T_{R,4}$	1345	1335
$T_{outlet,bottom}$	1390	1380



Modeling

The heat transfer model is formulated for the two sections of the TES, namely the sensible and latent heat storage sections. These are coupled by the conditions of the air flow at the interface ($h_{f,out,PCM}=h_{f,in,rocks}$) and the radiative exchange between them.

Sensible heat-storage section — The heat-transfer model developed by (Zanganeh et al., 2012) was adapted to the experimental setup described above. The model considers separate fluid and solid phases with variable thermo-physical properties, thermal losses from the walls, and axial dispersion by conduction and radiation. The governing equations are,

Fluid:

$$\varepsilon_{rocks} \rho_f V \frac{de_f}{dt} = A \varepsilon_{rocks} \left[(u \rho_f h_f)_{in} - (u \rho_f h_f)_{out} \right] + h_{v,eff,rocks} V (T_s - T_f) + Q_{wall,rocks} \quad (1)$$

Solid:

$$(1 - \varepsilon_{rocks}) \rho_s V \frac{de_s}{dt} = h_{v,eff,rocks} V (T_f - T_s) + A \left[\left(k_{eff} \frac{dT_s}{dx} \right)_{out} - \left(k_{eff} \frac{dT_s}{dx} \right)_{in} \right] \quad (2)$$

where all symbols are defined in the nomenclature.

Latent heat-storage section — Fig. 9 shows the relevant heat fluxes of this section. It is modeled following the approach of (Beasley et al., 1989). Instead of the effective axial dispersion as in Eq. (2), the conduction and radiation heat transfer are considered separately and included along with the wall source/sink term in the solid phase. The governing equations are:

Fluid:

$$\varepsilon_{PCM} \rho_f V \frac{de_f}{dt} = A \varepsilon_{PCM} \left[(u \rho_f h_f)_{in} - (u \rho_f h_f)_{out} \right] + h_{v,PCM} V (T_{PCM} - T_f) \quad (3)$$

PCM:

$$(1 - \varepsilon_{PCM}) (\rho C)_{eff} V \frac{dT_{PCM}}{dt} = h_{v,PCM} V (T_f - T_{PCM}) + Q_{cond,PCM} + Q_{rad,PCM} + Q_{wall,PCM} \quad (4)$$

The source terms and coefficients in Eq. (1) to (4) are explained in the next section.

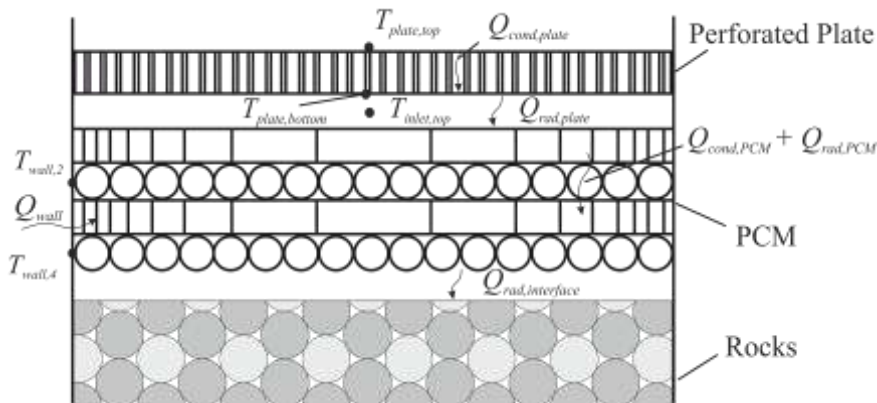


Fig. 9: PCM section showing the relevant heat fluxes.



Closure relations and boundary conditions — All parameters used in the equations stated below are listed in Table 6. The thermo-physical properties of air are calculated using high-order polynomial fits of tabulated data (Incropera et al., 2007). The convective heat transfer in the packed bed of rocks is calculated using the correlation of (Alanis et al., 1976), which was developed for similar particle sizes ($d=2.1-5.8$ cm), void fraction ($\varepsilon=0.421$), and Reynolds numbers ($10 < Re_0 < 200$) as encountered in the present work,

$$h_{v,rocks} = 824(G/d)^{0.92} \quad (5)$$

and adjusted to consider the intra-particle conduction with (Bradshaw et al., 1970; Beasley et al., 1989)

$$h_{v,eff,rocks} = \frac{h_{v,rocks}}{1 + 0.25Bi} \quad (6)$$

The effective thermal conductivity of the packed bed of rocks, k_{eff} , considers dispersion by conduction and radiation using correlations developed by (Kunii and Smith, 1960) and (Yagi and Kunii, 1957). The correlation for the convective heat transfer relevant to tubes in cross flow in the latent-heat section is due to (Zukauskas, 1972),

$$Nu_{PCM} = 0.51C_{row} Re^{0.5} Pr_f^{0.37} (Pr_f/Pr_s)^{0.25} \quad (7)$$

The above equation is valid for staggered tubes in cross flow and $100 < Re < 1000$. The coefficient C_{row} accounts for row numbers less than 20, as in the present experimental setup. Pr_f is the fluid Prandtl number evaluated at the fluid temperature and Pr_s the fluid Prandtl number evaluated at the solid temperature. In contrast to packed beds where the Reynolds number is generally based on the superficial velocity u_0 , the Reynolds number in Eq. (7) is based on the maximum interstitial velocity,

$$u_{max} = \frac{S_T}{S_D - d_{enc}} u_0 \quad (8)$$

with S_T and S_D the transverse and longitudinal pitch. The volumetric heat-transfer coefficient is obtained from

$$h_{v,PCM} = Nu_{PCM} k_f a_{PCM} / d_{enc} \quad (9)$$

where a_{PCM} is the surface area per unit volume of PCM. The inlet temperature, $T_{inlet,top}$, as shown in Fig. 9, is the temperature of the incoming air. Due to the high temperatures involved, the radiation exchange between the perforated plate and the first PCM row is taken into account using the methodology by (Siegel and Howell, 2002)

$$Q_{rad,plate} = \frac{\sigma A_{plate} (1 - \varepsilon_{plate}) (T_{plate,bottom}^4 - T_{PCM,1}^4)}{1/\delta_{plate} + 1/\delta_{enc} - 1} \quad (10)$$

where $\varepsilon_{plate} = \sum A_{holes} / A_{plate}$ is the void fraction of the perforated plate and temperatures are in Kelvin. Due to the high conductivity of the PCM and encapsulation, the tube surface temperature is taken equal to the PCM temperature as justified by the low Biot numbers in the PCM section ($Bi < 0.001$) and shown in Fig. 7. The emissivity of the plate and encapsulation is taken to be that for oxidized stainless steel (Incropera et al., 2007). $T_{plate,bottom}$ is obtained by applying an energy balance on the perforated plate. At any time step, the heat conducted through the plate, $Q_{cond,plate}$, is set equal to the heat that is radiatively exchanged with the PCM, $Q_{rad,plate}$

$$\frac{k_{plate} A_{plate} (1 - \varepsilon_{plate})}{t_{plate}} (T_{plate,top} - T_{plate,bottom}) = \frac{\sigma A_{plate} (1 - \varepsilon_{plate}) (T_{plate,bottom}^4 - T_{PCM,1}^4)}{1/\delta_{plate} + 1/\delta_{enc} - 1} \quad (11)$$

allowing $T_{plate,bottom}$ to be determined because $T_{plate,top}$ is measured during the experiments. The radiation exchange between the last PCM and first rocks layers is determined from



$$Q_{rad,interface} = \frac{\sigma A_{tank} (1 - \varepsilon_{PCM}) (T_{s,1}^4 - T_{PCM,4}^4)}{1/\delta_{enc} + 1/\delta_{rocks} - 1} \quad (12)$$

Eq. (2) is modified for the first layer to account for $Q_{rad,interface}$ by subtracting this term from its r.h.s. Eq. (4) is modified to account for $Q_{rad,plate}$ in the first layer and for $Q_{rad,interface}$ in the last layer by adding these terms to its r.h.s. For the “rocks only” setup, $Q_{rad,plate}$ is modified with data for rocks and added to the r.h.s. of Eq. (2) for the first layer. The conductive and radiative heat transfer between the PCM rows are accounted for separately and considered in the solid phase. The conductive heat transfer between the PCM rows is calculated from

$$Q_{cond,PCM} = A_{tank} f_{cont,PCM} \left[\left(k_{enc} \frac{dT_{PCM}}{dx} \right)_{out} - \left(k_{enc} \frac{dT_{PCM}}{dx} \right)_{in} \right] \quad (13)$$

where $f_{cont,PCM}$ is the estimated fraction of the tank cross section where the tubes are in physical contact. The presence of the caps with a slightly larger diameter than the tubes, as seen in Fig. 5, causes the tubes to touch only at their ends. Hence, the contact fraction is much less than $(1 - \varepsilon_{PCM})$. The radiative heat transfer between the PCM rows is

$$Q_{rad,PCM,i} = \frac{\sigma A_{tank} (1 - \varepsilon_{PCM})}{2/\delta_{enc} - 1} (T_{PCM,i+1}^4 - 2T_{PCM,i}^4 + T_{PCM,i-1}^4) \quad (14)$$

where i represents the row number that ranges from 1 to 4. For both Eq. (13) and (14), adiabatic conditions are applied at the inlet and outlet. For the “rocks only” setup, the radiative exchange between the plate and the rocks determined from Eq. (10).

The interaction of the storage materials with the walls is accounted for in the sensible heat storage section by considering thermal losses through the lateral walls in the fluid phase equation

$$Q_{wall,rocks} = h_{wall} A_c (T_{\infty} - T_f) \quad (15)$$

The overall wall heat-transfer coefficient, h_{wall} , considers the heat transfer between the packed bed and the wall with a convective term, as developed by (Beek, 1962), and a conductive/radiative term, as developed by (Ofuchi and Kunii, 1964), as well as the conductive heat transfer through the wall and insulation layers (Zanganeh et al., 2012). The outer surface temperature of the insulation, T_{∞} , is considered equal to the ambient temperature and invariant with time as verified by thermal images taken of the storage during operation. In the latent heat-storage section, the monitored wall temperature is used as a source/sink term with conductive heat transfer to/from the tubes

$$Q_{wall,PCM} = \frac{k_{enc} A_c f_{cont,wall}}{(r_{in} - t_{enc}) \ln\left(\frac{r_{in}}{r_{in} - t_{enc}}\right)} (T_{wall} - T_{PCM}) \quad (16)$$

While T_{wall} was measured for the 2nd and 4th row, linear extrapolation and interpolation was used in the model to obtain it for the 1st and 3rd row. $f_{cont,wall}$ is the fraction of the circumference that is in contact with the PCM tubes and is estimated visually from the experimental setup.



Table 6: Values of the parameters used in the Eq. (7) to (16). * Value known, measured, or calculated. † Value estimated.

A_{plate}^* [m ²]	0.122	ϵ_{plate}^* [-]	0.142	$\dot{\delta}_{plate}$ [-](Incropera et al., 2007)	0.7
A_{tank}^* [m ²]	0.122	$f_{cont,PCM}^\dagger$ [-]	0.05	$\dot{\delta}_{enc}$ [-](Incropera et al., 2007)	0.7
t_{plate}^* [m]	0.02	$f_{cont,wall}^\dagger$ [-]	0.02	$\dot{\delta}_{rocks}$ [-](Siegel and Howell, 2002)	0.83
t_{enc}^* [m]	0.001	S_T^* [m]	0.0253	C_{row} [-](Zukauskas, 1972)	0.95
k_{plate} [W/mK](Incropera et al., 2007)	41-35	S_D^* [m]	0.0253	a_{PCM} [m ² /m ³]*	103.45

The PCM showed a congruent phase trajectory of melting/solidification in the range of 573-577 °C, hence a melting temperature range ΔT_m of 4 °C. Following the approach by (Beasley et al., 1989), a pseudo-specific heat is introduced for this range

$$C_{pseudo} = h_{fus} / \Delta T_{melt} \quad (17)$$

The effective volumetric heat capacity in Eq. (4), $(\rho C)_{eff}$, is calculated as the volumetric average of the product of the heat capacity and the mass of the PCM and encapsulation

$$(\rho C)_{eff} = \frac{m_{PCM} C_{PCM} + m_{enc} C_{enc}}{V_{tubes}} \quad (18)$$

where V_{tubes} is the total volume of the encapsulation tubes in a row, m_{PCM} , m_{enc} , and V_{tubes} are row specific and given in Table 3, and C_{PCM} and C_{enc} are given in Table 4.

The small tank-to-particle diameter ratio of about 12 caused the void fraction to be larger close to the wall (Mueller, 1992; Ismail et al., 2002; Du Toit, 2008), which in turn resulted in a lower flow resistance and hence higher fluid velocities there (Schwartz and Smith, 1953; Newell and Standish, 1973; Chandrasekhara and Vortmeyer, 1979). According to (Schwartz and Smith, 1953), for tank-to-particle diameter ratios < 30, the peak velocity close to the wall can be 30 to 100% greater than the velocity at the center of the tube. (Hänchen et al., 2011) considered a bypass fraction of the flow and assumed that it bypasses the column without thermally interacting with the center of the packed bed. The same approach is used here with a bypass fraction of 15%, yielding good matching for all cases.

Numerical solution — The latent heat storage section is divided in 4 layers representing the four rows. The sensible heat storage section is divided in 64 and 68 layers for the “rocks + PCM” setup and “rocks only” setup, respectively. A grid size sensitivity analysis showed that further refinement did not affect the results. The fluxes at cell faces are approximated using a first-order approximation and the time derivatives are solved using the forward Euler method, resulting in explicit numerical schemes. Eq. (1) to (4) are solved for e_f , e_s , and T_{PCM} at the next time step. Air and rock temperatures are obtained using the temperature-dependent correlations for the internal energy of air and rocks, as presented above. The following initial and boundary conditions apply: 1) Adiabatic conditions for the fluid phase at the

outlet, i.e. $\frac{dh_f(x=H)}{dx} = 0$. 2) Adiabatic conditions for the solid phase at the inlet and outlet, i.e.

$\frac{dT_s(x=0)}{dx} = \frac{dT_s(x=H)}{dx} = 0$. 3) For the “rocks + PCM” setup during charging phase, the outlet fluid enthalpy of

the PCM section is used as the inlet condition for the rocks section ($h_{f,N,PCM} = h_{f,1,rocks}$), and vice versa during discharging.



Experimental Results and Model Validation

Table 7 summarizes the 4 experimental runs: runs #1 and #2 with the “rocks + PCM” setup and runs #3 and #4 with the “rocks only” setup. Runs #1 and #2 were carried out with similar mass flow rates and charging times as “rocks only” runs #3 and #4, respectively. Before the charging process, it was ensured that the storage was uniformly at ambient temperature ($T_{ambient} \approx 25$ °C). For all runs, the discharging process lasted until the storage was depleted to ambient temperature again.

Table 7: Summary of the experimental runs.

Run #	Setup	\dot{m}_{ch} [kg/s]	\dot{m}_{dis} [kg/s]	t_{ch} [h]
1	rocks + PCM	0.008-0.014	0.014	3:10
2	rocks + PCM	0.005-0.009	0.014	4:15
3	rocks only	0.008-0.014	0.014	3:10
4	rocks only	0.005-0.009	0.014	4:15

For runs #1 and #3, the heater power was ramped up until 95% of maximum heater power at a rate of 5% every 3 minutes and kept unchanged for the rest of the charging period. For runs #2 and #4, the heater power was ramped up until 70% of maximum heater power at a rate of 5% every 5 minutes and kept unchanged for the rest of the charging period. The Reynolds number in the sensible and latent heat storage sections were in the range 60-200 and 140-390, respectively. The Biot number range in the sensible and latent heat storage sections were in the range 0.04-0.24 and 0.0004-0.0011, respectively. Note that the low Biot number of the PCM is due to its high conductivity and that the effective convective heat transfer coefficient for the rocks is adjusted for intra-particle conduction with Eq. (6). The heat flows for the 4 experimental runs, calculated as the integral of the simulated heat fluxes over the charging and discharging periods, are summarized in Table 8.

Table 8: Simulated accumulated heat flows (in kWh) for the 4 experimental runs listed in Table 7.

Run #	E_{input}	$E_{rad,plate,ch}$	$E_{rad,plate,dis}$	$E_{wall,PCM,ch}$	$E_{wall,PCM,dis}$	$E_{wall,rocks,ch}$	$E_{wall,rocks,dis}$
1	18.4	0.95	-0.14	1.27	0.43	-0.24	-0.25
2	16.66	1.2	-0.11	1.3	0.67	-0.29	-0.21
3	19.3	1.01	0.42	-	-	-0.3	-0.3
4	16.09	1.15	0.33	-	-	-0.36	-0.25

Fig. 10 compares the bottom and top temperature profiles obtained from the experiments for the run #1 (“rocks + PCM” setup) and run #3 (“rocks only” setup). The bottom temperature profiles are similar for both cases indicating that the energy stored for both setups is comparable. Due to the presence of the melting regime for the “rocks + PCM” setup, the final top temperature of the charging period for this setup is about 10 °C lower than that for the “rocks only” setup. Although the outflow temperature during discharging drops faster initially for the “rocks + PCM” setup, a stabilization can be clearly observed. This in turn leads to the outflow temperature of the “rocks only” setup to drop below that of the “rocks + PCM” setup after about 70 minutes of discharging. The “rocks + PCM” setup stabilizes the outflow temperature for about 90 minutes after which all the PCM is solidified and the temperature begins to drop.

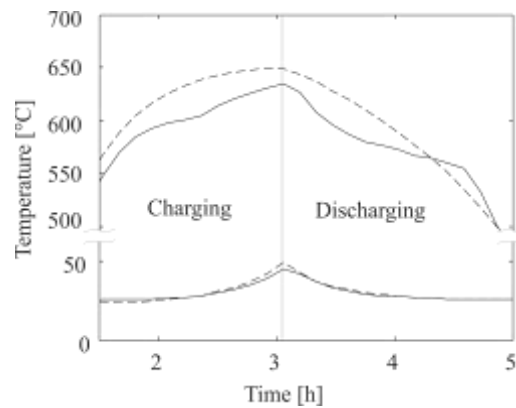


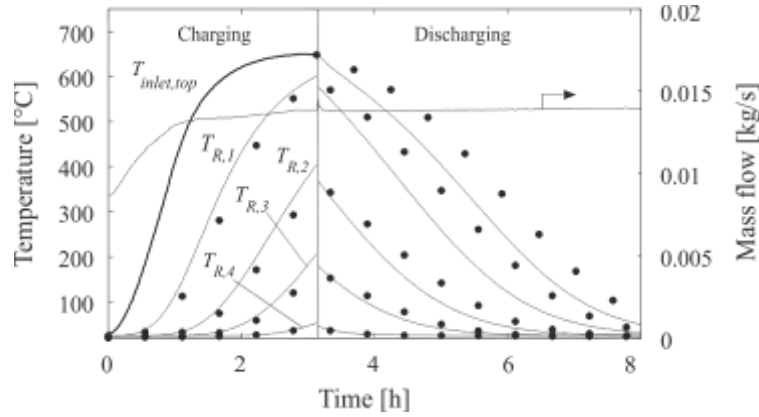
Fig. 10: Comparison of the experimentally obtained $T_{inlet,top}$ and $T_{outlet,bottom}$ for “rocks + PCM” run #1 (solid lines) and “rocks only” run #3 (dashed line).

Comparison of measured and simulated results for the four experimental runs (

Table 7) are shown in Fig. 11 and Fig. 12. For the packed bed of rocks, the simulated temperatures are taken to be averages of the solid and fluid temperatures. This is done as a simple heuristic correction to counter the effect of thermal radiation on the thermocouples, which appears as a decrease/increase the fluid temperature during charging/discharging. Fig. 11 shows the measured (markers) and simulated (curves) temperatures at various positions as a function of time during charging and discharging for the “rocks only” runs given by #3 and #4 in Table 7. Also indicated is the mass flow rate of air. For the charging phase, the agreement is reasonably good. For the discharging phase, the model predictions underestimate the measurements especially near the top of the tank. This is attributed to the thermal inertia of the tank and the release during discharging of the thermal energy stored in the insulation, which are not included in the model. This is the likely explanation for the larger discrepancies near the top where the temperatures are higher. The drop in the simulated results between charging and discharging is because of the inverted heat flow direction during discharging. While during charging the fluid temperature is higher than the solid temperature, during discharging, the solid is heating up the fluid and is therefore higher. Hence, there is a drop in the fluid temperature when the discharging starts, while the solid temperature has a smooth transition (see also Fig. 12 a) and b)). Consequently, the average temperature plotted in Fig. 10 also shows a drop. The thermal losses from the lateral walls, calculated from the model, are 3% and 3.5% of the total input energy during charging from the incoming air flow (E_{input}) and the radiative heat transfer from the perforated plate ($E_{rad,plate,ch}$) for runs #3 and #4, respectively. Due to the fast temperature drop of the simulation results during discharging, the net radiative heat transfer from the perforated plate to the packed bed, $E_{rad,plate,dis} > 0$, as shown in Table 8.



a)



b)

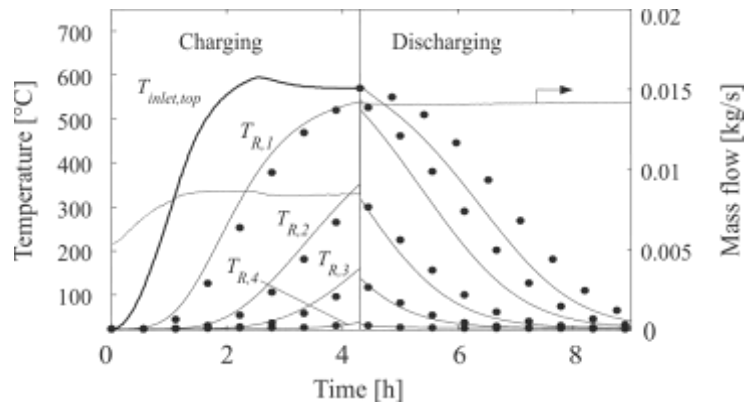


Fig. 11: Experimentally measured (markers) and simulated (curves) temperatures at various positions as a function of time during charging and discharging for the “rocks only” setup: a) run #3 ; b) run #4. Also indicated is the mass flow rate of air.

Fig. 12 shows the measured (markers) and simulated (curves) temperatures as a function of time during charging and discharging for the “rocks + PCM” setup: packed bed and inlet (top) temperatures for run #1 (a) and run #2 (b); PCM and air temperatures at 1st and 3rd row for run #1 (c) and run #2 (d). The overall agreement in the sensible portion of the storage is similar to that for runs 3 and 4 shown in Fig. 10. However, the discrepancy between the temperatures near the top of the storage is less pronounced during discharging than for runs 3 and 4. This is attributed to the storage wall temperature being measured in the PCM section and used as boundary condition in the model. For the sake of clarity, the 2nd and 4th PCM row are not shown. The difference between measured and simulated temperatures of the PCM and air is attributed on the convective heat-transfer correlation given by Eq. (7) that was derived for staggered tubes with parallel axes, whereas the tube axes are perpendicular in the present experiment. In addition, thermocouples are exposed to radiative heat exchange, which affects the reading when the surroundings are colder (during charging, the reading is lower than the actual air temperature) or hotter (vice versa during discharging). The faster solidification during the simulated discharging compared to the experimental results is attributed to the lower incoming temperatures from the packed bed of rocks in the model compared to the measurements. The dips in the simulated temperatures correspond to dips measured experimentally (visible especially in the fluid data points). They are caused by a PCM row starting or finishing changing its phase. When a PCM layer starts to melt, its temperature increase rate is reduced, due to $C_{pseudo} = h_{fus} / \Delta T_{melt}$ being much larger than C_{PCM} . This causes the second term on the right-hand side of Eq. (3) to become increasingly negative, and consequently decreases the rate with which the internal energy of the fluid increases. This decreasing rate is seen by the flattening of the temperature curve. Once the PCM is completely molten, the PCM temperature starts to increase rapidly, causing the second term on the right-hand side of Eq. (3) to increase to large

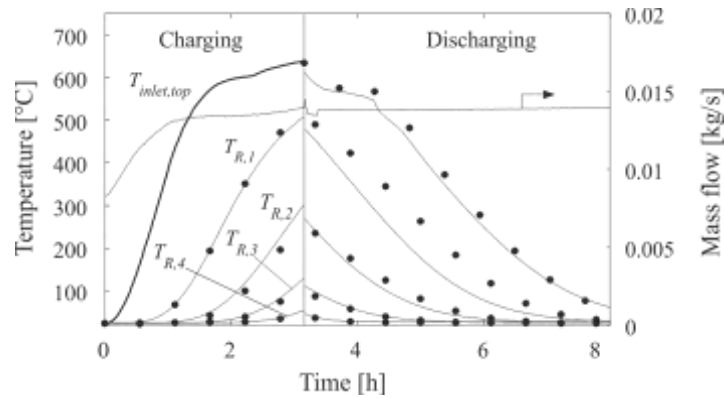
SFERA II - PROJECT



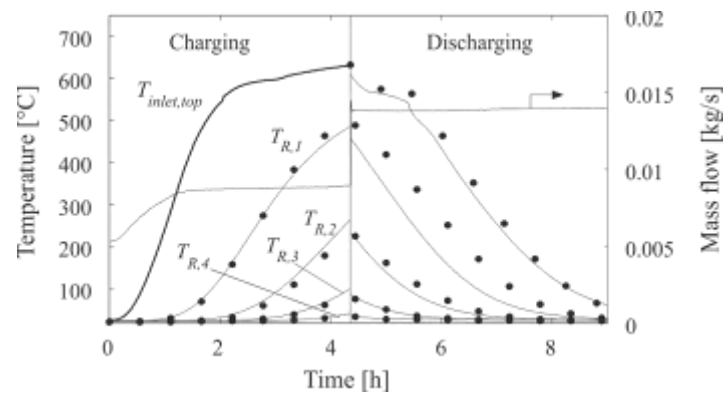
Solar Facilities for the European Research Area

positive values, which causes a sharp increase in the slope of the temperature curve. Due to radiation and conductive heat exchange across the PCM rows, these dips are seen in all rows when one of the PCM rows starts or finishes changing phase. The dips are also present during discharging, caused by the same mechanisms. The thermal losses from the lateral walls in the sensible section, as obtained by the simulation model, are 2.5% and 2.8% of the total input energy for runs #1 and #2, respectively. As shown in Table 8, due to the large thermal inertia of the insulation, the net integrated energy flow from the walls to the PCM during discharging, $E_{wall,PCM,dis} > 0$.

a)

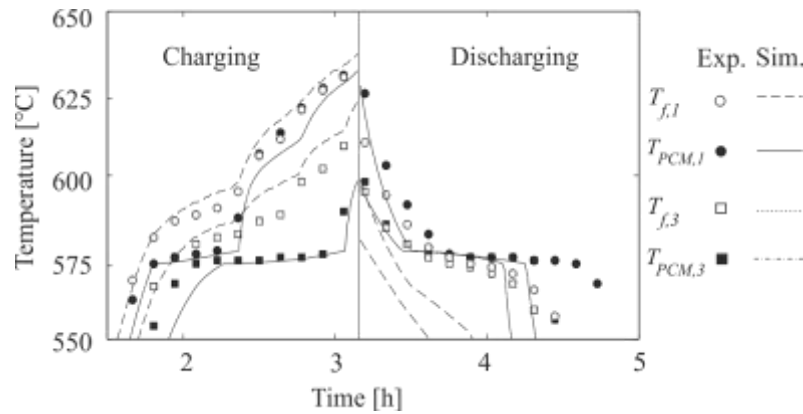


b)





c)



d)

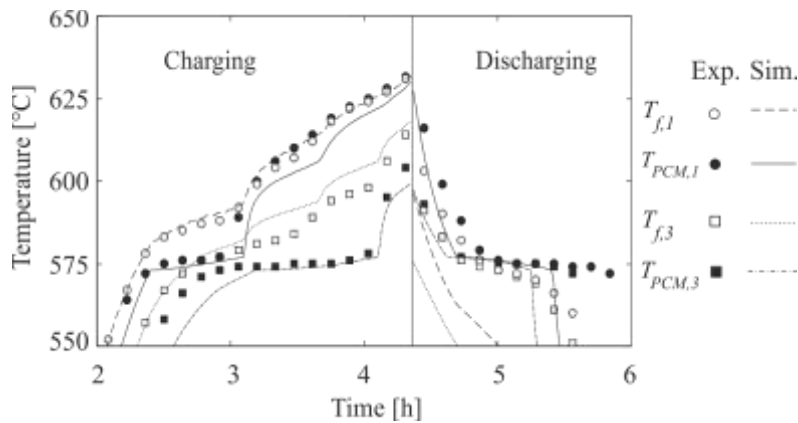


Fig. 12: Experimentally measured (markers) and simulated (curves) temperatures as a function of time during charging and discharging for the “rocks + PCM” setup: packed bed and inlet (top) temperatures for run #1 (a) and run #2 (b); PCM and air temperatures at 1st and 3rd row for run #1 (c) and run #2 (d).

Summary and Conclusions

An experimental and numerical analysis was carried out to investigate a 42 kWh_{th} lab-scale combined sensible and latent heat storage. The storage consisted of four rows of encapsulated PCM on top of a packed bed of rocks. AlSi₁₂ was used as PCM because its melting temperature of 575 °C is suitable for CSP applications, and because it has a high heat of fusion, high thermal conductivity, and low thermal expansion. AISI 316 stainless steel tubes were used as encapsulation. It was shown that the combined latent/sensible storage stabilizes the outflow air temperature around the melting temperature of AlSi₁₂ for approximately 90 minutes. The outflow air temperature was higher than in the sensible-storage-only case for a duration of about 20 minutes. A 1D transient model with variable fluid and solid properties was developed for the sensible- and latent-heat storage sections. Experimentally determined temperature-dependent thermo-physical properties of the rocks and PCM were used in the model. The model was validated with the experimental results. It was shown that the combined latent/sensible storage can stabilize the HTF outflow temperature around the melting temperature of the PCM while the PCM is partially molten. If the downstream application is a steam or gas turbine, the temperature stabilization might not be essential. It should nevertheless prove beneficial, however, because it allows the turbine to operate at its design point. On the other hand, if the downstream application is a chemical process, the stabilization might be crucial because it can ensure that the outflow temperature stays above the required reaction temperature.



References

- Agyenim, F., Hewitt, N., Eames, P., Smyth, M., 2010, A review of materials, heat transfer and phase change problem formulation for latent heat thermal energy storage systems (LHTESS), *Renewable and Sustainable Energy Reviews*, 14, 615-628.
- Alanis, E., Saravia, L., Rovetta, L., 1976, Measurement of Rock Pile Heat Transfer Coefficients, *Solar Energy*, 19, 571-572.
- Antony Aroul Raj, V., Velraj, R., 2011, Heat transfer and pressure drop studies on a PCM-heat exchanger module for free cooling applications, *International Journal of Thermal Sciences*, 50, 1573-1582.
- Arkar, C., Medved, S., 2005, Influence of accuracy of thermal property data of a phase change material on the result of a numerical model of a packed bed latent heat storage with spheres, *Thermochimica Acta*, 438, 192-201.
- Bader, R., Barbato, M., Pedretti, A., Steinfeld, A., 2010, An Air-Based Cavity-Receiver for Solar Trough Concentrators, *Journal of Solar Energy Engineering*, 132, 031017.
- Bader, R., Pedretti, A., Steinfeld, A., 2011, A 9-m-Aperture Solar Parabolic Trough Concentrator Based on a Multilayer Polymer Mirror Membrane Mounted on a Concrete Structure, *Journal of Solar Energy Engineering*, 133, 031016.
- Beasley, D.E., Clark, J.A., 1984, Transient response of a packed bed for thermal energy storage, *International Journal of Heat and Mass Transfer*, 27, 1659-1669.
- Beasley, D.E., Ramanarayanan, C., Torab, H., 1989, Thermal response of a packed bed of spheres containing a phase-change material, *International Journal of Energy Research*, 13, 253-265.
- Beek, J., 1962, Design of Packed Catalytic Reactors, *Advances in Chemical Engineering*, 3, 203-271.
- Birchenall, C.E., Riechman, A.F., 1980, Heat Storage in Eutectic Alloys, *Metallurgical Transactions*, 11A, 1415-1420.
- Boyd, D.A., Gajewski, R., Swift, R., 1976, A cylindrical blackbody solar energy receiver, *Solar Energy*, 18, 395-401.
- Bradshaw, A.V., Johnson, A., McLachlan, N.H., Chiu, Y.T., 1970, Heat transfer between air and nitrogen and packed beds of non-reacting solids, *Trans. Instn Chem. Engrs*, 48, T77.
- Buck, R., Abele, M., Kunberger, J., Denk, T., Heller, P., Lüpfer, E., 1999, Receiver for solar-hybrid gas turbine and combined cycle systems, *Le Journal de Physique IV*, 9, 537-544.
- Cárdenas, B., León, N., 2013, High Temperature Latent Heat Thermal Energy Storage: Phase Change Materials, Design Considerations and Performance Enhancement Techniques, *Renewable and Sustainable Energy Reviews*, 27, 724-737.
- Chandrasekhara, B.C., Vortmeyer, D., 1979, Flow Model for Velocity Distribution in Fixed Porous Beds Under Isothermal Conditions, *Wärme- und Stoffübertragung*, 12, 105-111.
- Coutier, J.P., Farber, E.A., 1982, Two applications of a numerical approach of heat transfer process within rock beds, *Solar Energy*, 29, 451-462.
- Du Toit, C.G., 2008, Radial Variation in Porosity in Annular Packed Beds, *Nuclear Engineering and Design*, 238, 3073-3079.
- Dutil, Y., Rousse, D.R., Salah, N.B., Lassue, S., Zalewski, L., 2011, A review on phase-change materials: mathematical modeling and simulations, *Renewable and Sustainable Energy Reviews*, 15, 112-130.
- Ettouney, H., El-Dessouky, H., Al-Ali, A., 2005, Heat transfer during phase change of paraffin wax stored in spherical shells, *Journal of Solar Energy Engineering*, 127, 357-365.
- Farid, M.M., Khudhair, A.M., Razack, S.A.K., Al-Hallaj, S., 2004, A review on phase change energy storage: materials and applications, *Energy Conversion and Management*, 45, 1597-1615.
- Fernandes, D., Pitié, F., Cáceres, G., Baeyens, J., 2012, Thermal energy storage: "How previous findings determine current research priorities", *Energy*, 39, 246-257.
- Flueckiger, S.M., Garimella, S.V., 2014, Latent heat augmentation of thermozone energy storage for concentrating solar power – A system-level assessment, *Applied Energy*, 116, 278-287.
- Flueckiger, S.M., Yang, Z., Garimella, S.V., 2012, Review of Molten-Salt Thermozone Tank Modeling for Solar Thermal Energy Storage, *Heat Transfer Engineering*, 34, 787-800.



- Fukai, J., Hamada, Y., Morozumi, Y., Miyatake, O., 2003, Improvement of thermal characteristics of latent heat thermal energy storage units using carbon-fiber brushes: experiments and modeling, *International Journal of Heat and Mass Transfer*, 46, 4513-4525.
- Geyer, M., Bitterlich, W., Werner, K., 1987, The Dual Medium Storage Tank at the IEA/SSPS Project in Almeria (Spain); Part I: Experimental Validation of the Thermodynamic Design Model, *Journal of Solar Energy Engineering*, 109, 192-198.
- Gil, A., Medrano, M., Martorell, I., Lázaro, A., Dolado, P., Zalba, B., Cabeza, L.F., 2010, State of the art on high temperature thermal energy storage for power generation. Part 1 - Concepts, materials and modellization, *Renewable and Sustainable Energy Reviews*, 14, 31-55.
- Good, P., Zanganeh, G., Ambrosetti, G., Barbato, M., Pedretti, A., Steinfeld, A., Towards a commercial parabolic trough CSP system using air as heat transfer fluid, *SolarPACES*, 17-20 September 2013, Las Vegas, USA
- Hahne, E., Taut, U., Gross, U., Salt Ceramic Thermal Energy Storage for Solar Thermal Central Receiver Plants, *Solar World Congress*, 1991, Denver (CO), USA
- Hänchen, M., Brückner, S., Steinfeld, A., 2011, High-temperature thermal storage using a packed bed of rocks – Heat transfer analysis and experimental validation, *Applied Thermal Engineering*, 31, 1798-1806.
- He, Q., Zhang, W., 2001, A study on latent heat storage exchangers with the high-temperature phase-change material, *International Journal of Energy Research*, 25, 331-341.
- Heller, P., Pfänder, M., Denk, T., Tellez, F., Valverde, A., Fernandez, J., Ring, A., 2006, Test and evaluation of a solar powered gas turbine system, *Solar Energy*, 80, 1225-1230.
- Hemingway, B.S., 1987, Quartz: Heat capacities from 340 to 1000 K and revised values for the thermodynamic properties, *American Mineralogist*, 72, 273-279.
- Herrmann, U., Geyer, M., Kearney, D., Overview on Thermal Storage Systems, *NREL Workshop on Thermal Storage for Trough Power Systems*, 20-21 February 2003, Golden, CO, USA
- Herrmann, U., Kearney, D.W., 2002, Survey of Thermal Energy Storage for Parabolic Trough Power Plants, *Journal of Solar Energy Engineering*, 124, 145-152.
- Hischier, I., Leumann, P., Steinfeld, A., 2012, Experimental and Numerical Analyses of a Pressurized Air Receiver for Solar-driven Gas Turbines, *ASME Journal of Solar Energy Engineering*, 134, 1-8.
- Incropera, F.P., Dewitt, D.P., Bergman, T.L., Lavince, A.S., 2007, *Fundamentals of Heat and Mass Transfer*, 6th ed., John Wiley & Sons, Hoboken, NJ.
- Ismail, J.H., Fairweather, M., Javed, K.H., 2002, Structural Properties of Beds Packed with Ternary Mixtures of Spherical Particles, Part II - Local Properties, *Trans IChemE*, 80, 645-653.
- Jakiel, C., Zunft, S., Nowi, A., 2007, Adiabatic compressed air energy storage plants for efficient peak load power supply from wind energy: the European project AA-CAES, *International Journal of Energy Technology and Policy*, 5, 296-306.
- Jalalzadeh-Azar, A.A., Steele, W.G., Adebisi, G.A., 1996, Heat Transfer in a High-Temperature Packed Bed Thermal Energy Storage System - Roles of Radiation and Intraparticle Conduction, *Journal of Energy Resources Technology*, 118, 50-57.
- Jalalzadeh-Azar, A.A., Steele, W.G., Adebisi, G.A., 1997, Performance comparison of high temperature packed bed operation with PCM and sensible heat pellets, *International Journal of Energy Research*, 21, 1039-1052.
- Jones, B.W., Golshekan, M., 1989, Destratification and other properties of a packed bed heat store, *International Journal of Heat and Mass Transfer*, 32, 351-359.
- Kenisarin, M., Mahkamov, K., 2007, Solar energy storage using phase change materials, *Renewable and Sustainable Energy Reviews*, 11, 1913-1965.
- Kenisarin, M.M., 2010, High-temperature phase change materials for thermal energy storage, *Renewable and Sustainable Energy Reviews*, 14, 955-970.
- Kolb, G.J., Alpert, D.J., Lopez, C.W., 1991, Insights from the operation of Solar One and their implications for future central receiver plants, *Solar Energy*, 47, 39-47.



- Kotzé, J.P., Backström, T.W., Erens, P.J., Simulation and testing of a latent heat thermal energy storage unit with metallic phase change material, SolarPACES, 17-20 September 2013a, Las Vegas, USA
- Kotzé, J.P., Backström, T.W.v., Erens, P.J., 2013b, High Temperature Thermal Energy Storage Utilizing Metallic Phase Change Materials and Metallic Heat Transfer Fluids, *Journal of Solar Energy Engineering*, 135, 1-6.
- Kribus, A., Doron, P., Rubin, R., Reuven, R., Taragan, E., Duchan, S., Karni, J., 2001, Performance of the Directly-Irradiated Annular Pressurized Receiver (DIAPR) operating at 20 bar and 1200 C, *Journal of Solar Energy Engineering*, 123, 10-17.
- Kunii, D., Smith, J.M., 1960, Heat transfer characteristics of porous rocks, *A.I.Ch.E. Journal*, 6, 71-78.
- Kuravi, S., Trahan, J., Goswami, Y., Rahman, M., Stefanakos, E., 2013, Thermal energy storage technologies and systems for concentrating solar power, *Progress in Energy and Combustion Science*, 39, 285-319.
- Medrano, M., Gil, A., Martorell, I., Potau, X., Cabeza, L.F., 2010, State of the art on high-temperature thermal energy storage for power generation. Part 2 - Case studies, *Renewable and Sustainable Energy Reviews*, 14, 56-72.
- Meier, A., Winkler, C., Wuillemin, D., 1991, Experiment for modelling high temperature rock bed storage, *Solar Energy Materials*, 24, 255-264.
- Michels, H., Pitz-Paal, R., 2007, Cascaded latent heat storage for parabolic trough solar power plants, *Solar Energy*, 81, 829-837.
- Mueller, G.E., 1992, Radial Void Fraction Distributions in Randomly Packed Fixed Beds of Uniformly Sized Spheres in Cylindrical Containers, *Powder Technology*, 72, 269-275.
- Nallusamy, N., Sampath, S., Velraj, R., 2007, Experimental investigation on a combined sensible and latent heat storage system integrated with constant/varying (solar) heat source, *Renewable Energy*, 32, 1206-1227.
- Newell, R., Standish, N., 1973, Velocity Distribution in Rectangular Packed Beds and Non-Ferrous Blas Furnaces, *Metallurgical Transactions*, 4, 1851-1857.
- Nkwetta, D.N., Haghightat, F., 2014, Thermal energy storage with phase change material - A state-of-the art review, *Sustainable Cities and Society*, 10, 87-100.
- Nsofor, E.C., Adebisi, G.A., 2001, Measurements of the gas-particle convective heat transfer coefficient in a packed bed for high-temperature energy storage, *Experimental Thermal and Fluid Science*, 24, 1-9.
- Ofuchi, K., Kunii, D., 1964, Heat-transfer characteristics of packed beds with stagnant fluids, *International Journal of Heat and Mass Transfer*, 8, 749-757.
- Pitz-Paal, R., Amin, A., Oliver Bettzuge, M., Eames, P., Flamant, G., Fabrizi, F., Holmes, J., Kribus, A., van der Laan, H., Lopez, C., Garcia Novo, F., Papagiannakopoulos, P., Pihl, E., Smith, P., Wagner, H.-J., 2012, Concentrating Solar Power in Europe, the Middle East and North Africa: A Review of Development Issues and Potential to 2050, *Journal of Solar Energy Engineering*, 134, 024501-024501.
- Pratten, N.A., 1981, The precise measurement of the density of small samples, *Journal of Materials Science*, 16, 1737-1747.
- Reilly, H.E., Kolb, G.J., 2001, An Evaluation of Molten-Salt Power Towers Including Results of the Solar Two Project, SANDIA National Laboratories,
- Schwartz, C.E., Smith, J.M., 1953, Flow Distribution in Packed Beds, *Industrial and Engineering Chemistry*, 45, 1209-1218.
- Shitzer, A., Levy, M., 1983, Transient behavior of a rock-bed thermal storage system subjected to variable inlet air temperatures: Analysis and experimentation, *Journal of Solar Energy Engineering*, 105, 200-206.
- Siegel, R., Howell, J., 2002, *Thermal Radiation Heat Transfer*, 4th ed., Taylor & Francis, New York.
- SOLUCAR, 2006, PS10: A 11.0 MWe solar tower power plant with saturated steam receiver, SOLUCAR,
- Somerton, W.H., 1992, *Thermal properties and temperature-related behavior of rock/fluid systems*, Elsevier, New York NY.
- Sorour, M.M., 1988, Performance of a small sensible heat energy storage unit, *Energy Conversion and Management*, 28, 211-217.

SFERA II - PROJECT



Solar Facilities for the European Research Area

- Valmiki, M., Karaki, W., Peiwen, L., Van Lew, J., Cholik, C., Stephens, J., 2012, Experimental Investigation of Thermal Storage Processes in a Thermocline Tank, *Journal of Solar Energy Engineering*, 134, 041003.
- Van Lew, J.T., Peiwen, L., Chan, C.L., Karaki, W., Stephens, J., 2011, Analysis of heat storage and delivery of a thermocline tank having solid filler material, *Journal of Solar Energy Engineering*, 133, 021003.
- Wang, X., Liu, J., Zhang, Y., Di, H., Jiang, Y., 2006, Experimental research on a kind of novel high temperature phase change storage heater, *Energy Conversion and Management*, 47, 2211-2222.
- Warerkar, S., Schmitz, S., Goettsche, J., Hoffschmidt, B., Reißel, M., Tamme, R., 2011, Air-Sand Heat Exchanger for High-Temperature Storage, *Journal of Solar Energy Engineering*, 133, 021010.
- Watanabe, T., Kikuchi, H., Kanzawa, A., 1993, Enhancement of charging and discharging rates in a latent heat storage system by use of PCM with different melting temperatures, *Heat Recovery Systems and CHP*, 13, 57-66.
- Wipware, 2013, Online Photoanalysis Service.
- Yagi, J., Akiyama, T., 1995, Storage of thermal energy for effective use of waste heat from industries, *Journal of Materials Processing Technology*, 48, 793-804.
- Yagi, S., Kunii, D., 1957, Studies on effective thermal conductivities in packed beds, *A.I.Ch.E. Journal*, 3, 373-381.
- Yang, L., Zhang, X., 2012, Performance of a new packed bed using stratified phase change capsules, *International Journal of Low-Carbon Technologies*, 7, 208-214.
- Zalba, B., Marín, J.M., Cabeza, L.F., Mehling, H., 2003, Review on thermal energy storage with phase change: materials, heat transfer analysis and applications, *Applied Thermal Engineering*, 23, 251-283.
- Zanganeh, G., Commerford, M., Haselbacher, A., Pedretti, A., Steinfeld, A., 2014, Stabilization of the outflow temperature of a packed-bed thermal energy storage by combining rocks with phase change materials, *Applied Thermal Engineering*, 70, 316-320.
- Zanganeh, G., Pedretti, A., Zavattoni, S., Barbato, M., Steinfeld, A., 2012, Packed-bed thermal storage for concentrated solar power - Pilot-scale demonstration and industrial-scale design, *Solar Energy*, 86, 3084-3098.
- Zukauskas, A., 1972, Heat Transfer from Tubes in Crossflow, *Advances in Heat Transfer*, 8, 93-160.
- Zunft, S., Hänel, M., Krüger, M., Dreißigacker, V., Göhring, F., Wahl, E., 2011, Jülich Solar Power Tower—Experimental Evaluation of the Storage Subsystem and Performance Calculation, *Journal of Solar Energy Engineering*, 133, 031019.